Efficiency Enhancement of Cadmium Telluride Solar Cells via Nanoengineering

BY

RADE KULJIC
B.S., University of Illinois at Urbana-Champaign, 2009

THESIS

Submitted as partial fulfillment of the requirements
for the degree of Master of Science in Electrical and Computer Engineering
in the Graduate College of the
University of Illinois at Chicago, 2011

Chicago, Illinois

Committee members:
Mitra Dutta, Chair and Advisor
Michael Stroscio
Seth Darling, Argonne National Laboratory

ACKNOWLEDGEMENTS

I would like to thank many people who have helped me while pursuing my degree. Their contribution to this work was enormous.

First of all, I would like to express my gratitude to my advisor, Prof. Mitra Dutta for her support, knowledge, patience, encouragement, and great professional opportunities provided to me during my graduate studies. This work would not be possible without her advice.

Thanks to my committee members Prof. Michael Stroscio and Seth Darling for reviewing this work and giving me helpful suggestions. Special thanks to Seth Darling for his support and guidance during my research in the Center for the Nanoscale Materials (CNM), Argonne National Laboratory.

Thanks to my research colleagues in the NanoEngineering Research Laboratory for their support and friendship: Hyeson Jung, Banani Sen, Ayan Kar, and Mohsen Purahmad. Also, thanks to postdocs at the CNM, Argonne National Laboratory, for their guidance and friendship: Yu-Chih Tseng, Wei Chen, and Maxim Nikiforov.

Last but not the least, I would like to thank to my family and friends for their support and encouragement.

RK

TABLE OF CONTENTS

TABLE OF CONTENTS (continued)

LIST OF TABLES

LIST OF FIGURES

LIST OF FIGURES (continued)

LIST OF FIGURES (continued)

LIST OF ABBREVIATIONS

AFM	Atomic Force Microscopy
ATR FTIR	Attenuated Total Reflectance Fourier Transform Infrared
BCP	Block Copolymer Lithography
EDX	Energy Dispersive X-ray
FRET	Fluorescence Resonant Energy Transfer.
ITO	Indium Tin Oxide
MEG	Multiple Exciton Generation
ODT	Order-Disorder Temperature
PL	Photoluminescence
PS-b-PMMA	poly(styrene-*block*-methyl methacrylate)
QDs	Quantum Dots
RCP	Random Copolymer
RIE	Reactive Ion Etching
TCO	Transparent Conductive Oxide

SUMMARY

Polycrystalline thin film solar cells based on cadmium-telluride (CdTe) have been studied in nonstandard cell configurations; a nanocrystalline layer of self-assembled quantum dots (QDs) was inserted into the standard cell structure in order to explore nontraditional approaches for efficiency enhancement including plasmonic effects, photon energy conversion, multiple exciton generation (MEG), and fluorescence resonant energy transfer (FRET). In addition, the block copolymer (BCP) lithography approach has been investigated in order to assemble uniform and closely packed metallic nanostructured arrays on transparent conductive oxide (TCO) substrates, desirable in a number of photovoltaic applications.

The CdTe solar cell structures were grown by vacuum deposition techniques followed by annealing treatments. The nanocrystalline layers were applied by drop-casting. A home built cadmium chloride ($CdCl_2$) vapor process was utilized for activation of the cell junctions.

Three types of cell structures were fabricated: two nonstandard structures, one with the nanocrystalline layer inserted into the junction, between the buffer and absorber, and the other one with the nanocrystalline layer fabricated between the front contact and the buffer layer; the third structure was the standard CdTe cell configuration which served as the control. Furthermore, the nanocrystalline layers were fabricated in three variations for each of the nonstandard structures, consisting of gold (Au), cadmium-sulfide (CdS), and cadmium-selenide (CdSe) QDs.

The cells were fabricated on 25 mm x 25 mm x 3 mm glass substrates coated with fluorine-doped tin oxide (SnO_2:F) from one side which served the purpose of the front electrode. Each substrate included a hundred devices of dimensions 2 mm x 2 mm ordered in a 10 x 10 matrix. The structures were characterized using photoluminescence spectroscopy (PL), optical microscopy, energy dispersive X-ray spectroscopy (EDX), and current-voltage (I-V) measurements.

The efficiency of the control devices was only around 2 % due to the nonoptimized home-built setup for the $CdCl_2$ treatment. Fabrication of the nanocrystalline layers proved to be difficult due to lack of adhesion caused by the higher temperature processes associated with the fabrication; formation of irregular nano and microclusters in the nanocrystalline layer rather than regular arrays of nanoparticles seemed to contribute to the adhesion issues. As a result, the nonstandard devices featured much smaller efficiencies or even total destruction of the structures. A conflicting relation of the annealing durations has been observed: longer annealing times were desirable for the $CdCl_2$ treatment, while shorter annealing times were necessary to avoid the adhesion issues.

In the study on nanostructured arrays assembled via BCP lithography, nanoengineering of Au particles on indium tin oxide (ITO) substrate has been investigated. In this work, poly(styrene-*block*-methyl methacrylate) block copolymer, known as PS-*b*-PMMA, was used to obtain a nanoporous template to be used as a sacrificial layer for fabrication of the Au nanoparticles.

Application of PS-*b*-PMMA films was done by spin-coating, after neutralizing the substrate surface with a random copolymer (RCP). This step was followed by an annealing treatment in order to induce phase separation of the blocks. Removal of the PMMA blocks from the polystyrene (PS) matrices was performed by reactive ion etching (RIE) in oxygen plasma, followed by a wet chemical treatment. As a result, nonporous films of PS with highly ordered and closely packed nanopores were obtained. An ultra-thin film of gold (Au) was deposited over the obtained templates using an e-beam evaporation system. The lift-off process considering a number of chemicals is currently under investigation. The structures were characterized using atomic force microscopy (AFM), attenuated total reflectance Fourier transform infrared spectroscopy (ATR FTIR), and energy dispersive X-ray spectroscopy (EDX).

The Au nanostructured arrays on ITO will be utilized for the fabrication of nanoengineered hybrid CdS/polymer solar cells. They will serve the purpose of a catalyst for the growth of highly ordered vapor-liquid-solid (VLS) growth of CdS nanopillars that will be subsequently surrounded with a conjugated polymer. In addition, the nanostructured arrays may be optimized to serve as nanocrystalline layers in the nonstandard CdTe structures, since they are expected to be more robust with respect to adhesion issues due to their regularity.

1. INTRODUCTION

1.1. Why alternative energy?

Nowadays it is hard to imagine life without modern technology, which heavily influences the way we communicate, do business, travel, entertain, diagnose and treat illnesses, etc. A major prerequisite for the modern style of life is existence of sustainable and inexpensive energy sources. Without affordable electricity, oil, and gas resources, we simply would not be able to exploit most of the advantages provided to us by new technologies.

The majority of world economies rely on oil and other fossil fuels as the primary energy sources. However, global population growth along with rapid development of underdeveloped countries has significantly increased the energy demand in the last two decades. According to a number of studies, the growing trend of energy demand will continue in the future (Figure 1)[1] while crude oil resources will continue to rapidly decline. The present scenario, if maintained, will result in insufficient and expensive supply of energy preventing further economic prosperity. Therefore, from the economic point of view, it is necessary to replace fossils with alternative energy sources.

Another equally important motivation to switch to alternative sources of energy is the environment. Greenhouse emissions released in the atmosphere by combustion of carbon-containing fossil fuels cause air pollution and enhance global warming. Heavy consumption of fossils could result in significant climate change in the relatively near future, severely affecting wellbeing of all living species on our planet.

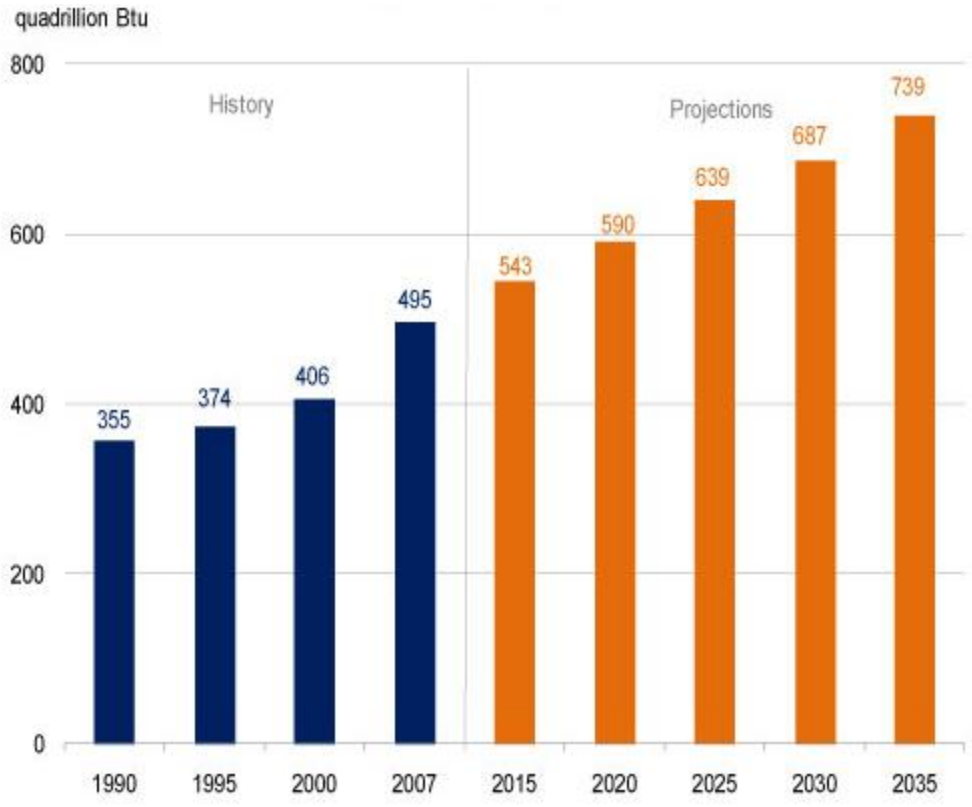

Figure 1. Global energy consumption from 1990 to 2035. Source: U.S. Energy Information Administration: http://www.eia.gov/oiaf/ieo/world.html

1.2. Why solar energy?

In order to overcome the energy deficit in the future, a number of alternative energy sources are considered. Most common types include nuclear, hydro, solar, wind, geothermal energy, and biomass fuels. Each of these options has certain advantages and disadvantages over the others and it is very likely that a combination of alternatives rather than a single source will be utilized in future global energy production. However, in

order to optimize future energy supply from the economic, environmental, and technical perspectives, it is necessary to identify and compare specific characteristics of each of the alternatives.

Nuclear energy, even though a well-developed, an economically efficient and a controllable means of power production, is associated with a number of health, safety and security concerns related to nuclear waste management, natural disasters, terrorist attacks, etc. Hydro, wind and geothermal power are renewable energy sources but are limited by geographical conditions and thus are not capable of expanding enough to provide a sufficient energy supply by themselves. Most of the world's locations with hydro and geothermal potentials are already being exploited, while wind energy is associated with high capital costs.[2] Biomass fuels are accompanied with greenhouse emissions during their production while the process of their extraction is very expensive.

Solar energy is renewable and carbon-free and is the most abundant energy source.[3] Currently, solar cells are not economically competitive with fossil fuels due to either their relatively low power conversion efficiencies or high manufacturing costs. However, conversion efficiencies of many commercialized solar devices are still well below their theoretical limits, thus leaving room for improvement, while different approaches to reduce manufacturing costs are being investigated. Therefore, solar energy has a significant potential to provide a sustainable, economically feasible, safe and environmentally friendly energy supply.

1.3. Solar technology market trends

The history of solar technology can be divided into three generations of solar cells. Each generation is characterized by a strategy approached from either a technical or economic point of view, pursued with a single ultimate goal – to minimize production costs of solar energy. This is a very challenging goal because of the trade-off between power conversion efficiency and manufacturing costs. One of the two major strategies, if not both, is generally applied to each of the three generations of cells in order to optimize this trade-off. The first strategy emphasizes improvement of power conversion efficiency at expense of material and manufacturing costs, while the second strategy puts an emphasis on reduction of material and fabrication expenses at the cost of lower efficiency.

The first generation solar cells include single-crystal silicon and gallium-arsenide p-n junction based photovoltaics. These are well-understood materials with well-established theoretical models and very controllable manufacturing processes. High quality single-crystal films are characterized with low level of defects implying minimized losses and high conversion efficiencies. However, the required high energy and labor inputs associated with these devices limit significant progress in lowering costs of energy production. Additionally, the first generation devices are reaching their theoretical limits of efficiency, thus not having potential for further performance improvements. Currently, these cells dominate the solar market with over 85% of solar energy production, but because of the mentioned limitations, they are not promising candidates for the future solar market.

The second generation cells, produced as a response to high manufacturing costs of the first generation, focus on the reduction of high energy and labor inputs and amounts of materials used. It includes p-n junction based thin film devices such as cadmium-telluride (CdTe), copper-indium-gallium-selenide (CIGS), amorphous silicon (a-Si), microcrystalline silicone (μc-Si) cells, etc. Relatively thick films characteristic for the first generation have been replaced by significantly thinner films, thus decreasing amount of material consumed. Also, high temperature processes have been eliminated where possible, and alternative, inexpensive deposition techniques were developed and applied. As a result, manufacturing costs are substantially reduced but power conversion efficiencies are inferior due to lower quality of films, which results in produced high energy cost. However, the theoretical efficiency limits of these devices are far above current levels leaving a potential for improvement. Assuming operation close to the theoretical limits, second generation solar cells might become an economically favorable option. These cells recently entered the solar panel market showing a trend to dominate in the near future.

The third generation of solar cells consists of nanocrystalline cells on one side, and organic and dye-sensitized solar cells on the other side. Certain theoretical concepts are considered for the design of nanocrystalline cells that allow for a more efficient utilization of the solar spectrum than in the case of homo-junction devices. The optimization of parameters such as charge generation and separation, band gap, molecular mass, molecular energy levels, molecule-to-molecule interactions, etc., has a potential to enhance efficiencies and overcome theoretical limits of single energy threshold devices. Main approaches in the nanocrystalline cell designs are:

- Utilization of materials or cell structures incorporating several band gaps
    - Multi-junction/tandem cells
    - Intermediate band cells
- Reduction of losses due to thermalization
    - Hot carrier extraction - hot carrier solar cells
    - Impact ionization – Multiple Exciton Generation (MEG) enhanced cells
- Photon energy conversion prior to absorption in a solar cell
    - Up-conversion cells
    - Down-conversion cells
- Light trapping
    - Plasmonic solar cell
- Fluorescence Resonant Energy Transfer (FRET)

Multi-junction cells currently hold the efficiency record and already have commercial applications in powering satellites. It is expected that these cells will eventually become cost effective when combined with solar concentrators. However, one of the major drawbacks of multi-junction cells is the higher fabrication costs due to a larger number of processing steps. Other nanocrystalline cells are still in the research phase, not yet with results worthy of commercialization but with a potential for improvements in the future.

Polymer and dye-sensitized solar cells belong to another subgroup of the third generation devices that primarily focus on material and fabrication cost reductions. These are emerging solar devices characterized by low cost materials used and nontraditional, inexpensive, processing with high throughput such as conventional printing, spin-coating,

spraying, and roll-to-roll techniques. Additionally, these are flexible and light weight devices that can be applied on a variety of substrates. However, these cells suffer from very low conversion efficiencies, up to 8 %, which currently makes them cost ineffective, even though they are being commercialized for some low power applications. Another issue related to these cells is material instability over a long term under operating conditions.[4] Future performance improvements would potentially make this class of devices a significant, if not dominant, contributor to the solar energy market.

1.4. Photovoltaic achievements of CdTe

Cadmium telluride solar cells are one of the major representatives of the second-generation thin film technologies. The development of these photovoltaics started in 1972 with introduction of a 6% efficient device and improved progressively until 2002 when researches at the *National Renewable Energy Laboratory* (NREL) set the current record efficiency of 16.7% (Figure 2). The theoretical efficiency limit for CdTe cells is close to 30%. Unfortunately, there have not been any performance improvements in the last nine years due to a lack of research in the device activation treatment[5] and the application of more sophisticated concepts.

Nevertheless, CdTe cells are currently commercialized by three major manufacturers, *Antec Solar* in Germany and *First Solar* and *Abound Solar* in the United States. Furthermore, *General Electric* recently announced its plans to build the largest US manufacturing solar panel plant.[6] Definitely, CdTe devices have a potential to become one of the most cost-efficient photovoltaics in the near future.

Further performance improvements of CdTe photovoltaics could contribute enormously to their success. The fact that CdTe possesses many good characteristics for photovoltaic applications, that its current efficiency levels are well below the theoretical limits, and that there has been no performance improvement during the last decade, were the main motivation of this work in order to consider an alternative way for the improvement inefficiency – nanoengineering.

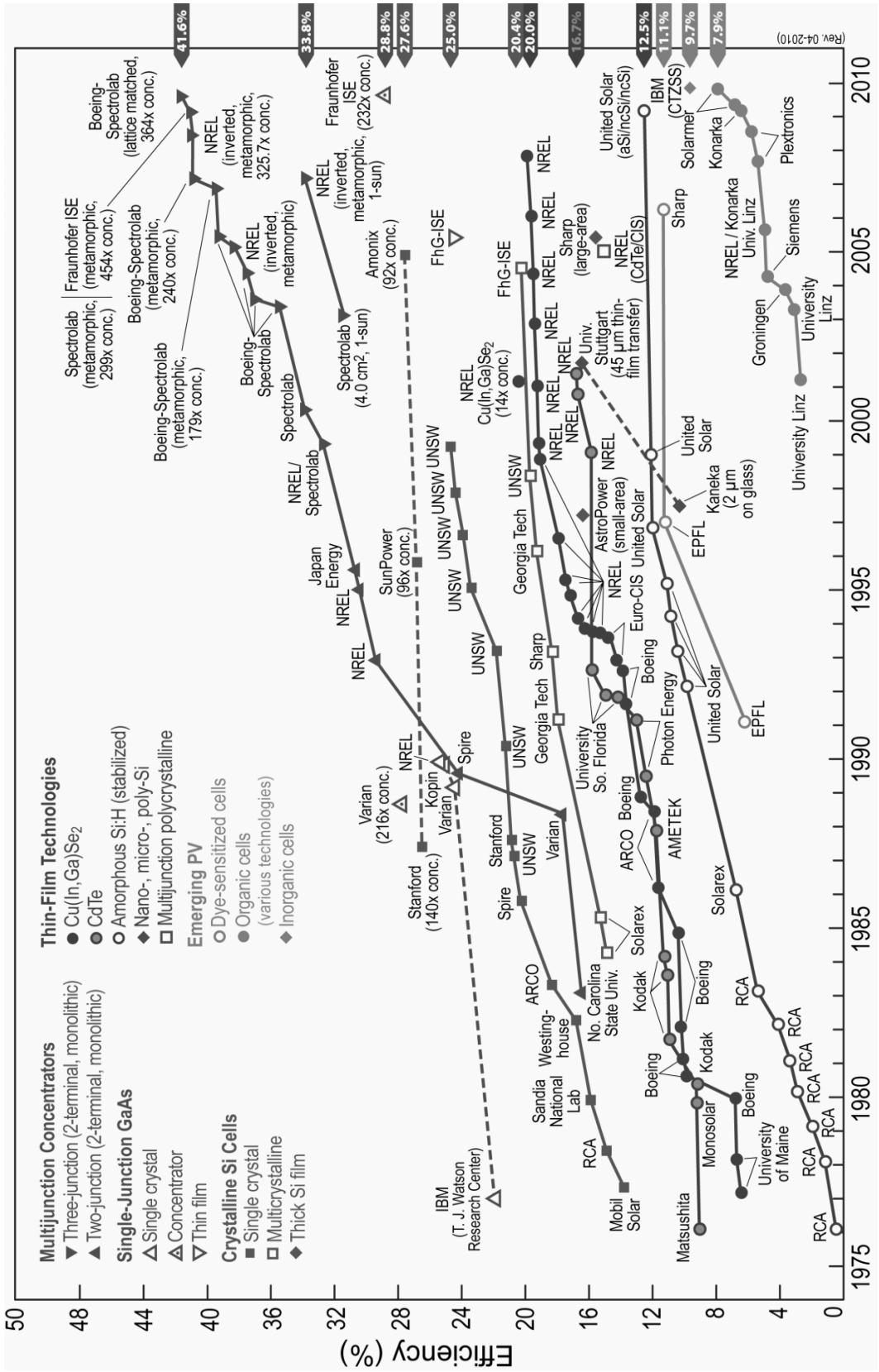

Figure 2. Progress in record efficiency of solar cells. Source: The United States Department of Energy
http://ferekide.blog.usf.edu/background-of-cadmium-telluride-cdte-thin-film-photovoltatic-cells/

2. BACKGROUND

2.1. Electrical properties of solid materials

Every atom has a set of discrete energy levels that can be occupied by electrons. As several atoms are brought together in close proximity, which is the case in solid materials, the original energy levels spread into energy bands. The highest occupied energy band is defined as the valence band, while the lowest unoccupied band is referred to as the conduction band. The region between the conduction band and the valence band is the forbidden region of energy for charge carriers and it is defined as the energy bandgap.

An electron in the valence band is strongly tied to the atom and it is not capable of conducting current unless it is excited to the conduction band via thermal energy or photons. In order for this to happen, the electron needs to absorb energy equal to or greater to the bandgap energy. Once it reaches the conduction band, the electron is able to move through many unoccupied states and thus conduct current. Therefore, the size of the bandgap plays a major role in determining electrical characteristics of materials.

Based on this criterion, materials are classified as conductors, semiconductors, or insulators (Figure 3). In the case of conductors, the conduction and the valence band overlap and there is no bandgap, which implies a good conduction property. In semiconductors, bandgap is of moderate size so these materials are poor conductors under usual circumstances; however, under external excitation (thermal energy, light, etc.), electrons are able to transition from the valence to the conduction band and promote conduction of electrical current. Similarly, in doped semiconductors, electrons from the

donor energy level near the conduction band, or holes from the acceptor energy level near the valence band need to absorb only a small amount of energy to be excited to the conduction band and the valence band respectively; thus, the doped semiconductors have good conducting property even at room temperature. Finally, insulators are characterized by a large bandgap where only a few electrons are able to be excited at the conduction band even under external excitation, which explains their poor electrical properties.

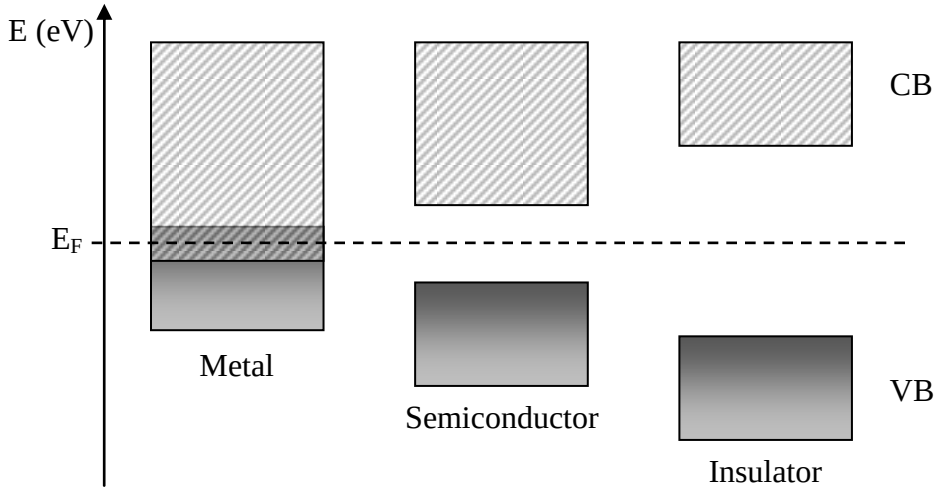

Figure 3. Energy band diagram of metals, semiconductors and insulators.

2.2. Photovoltaic effect

The mechanism responsible for conversion of solar energy into electrical energy is called the photovoltaic effect. Energy of light is transmitted by photons, small packets or "quanta" of light usually measured in electron-volts (eV). Energy of a photon depends

only on the characteristic frequency of the light and can be described by the equation $E = hf = hc/\lambda$, where h is Planck's constant, and $f, c,$ and λ are frequency, speed, and wavelength of light, respectively. Sunlight is composed from a spectrum of frequencies rather than from a single frequency (Figure 4), meaning that it contains photons of a whole range of energies.

When a photon interacts with an electron from a solid material, energy will be transferred into the electron's kinetic energy only if it is greater than the bandgap energy of the material. In this case, the electron is able to move through a number of unoccupied energy states and if an electric field is applied, it can be collected at an electrode, meaning that the photovoltaic conversion occurs. In the case of insufficient photon energy, the electron cannot enter the conduction band and conduct current, thus photovoltaic conversion does not happen.

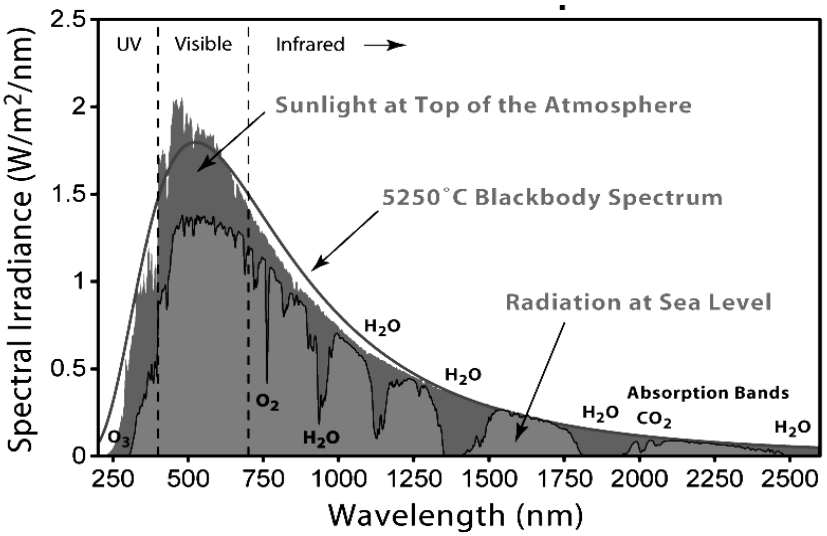

Figure 4. Solar radiation spectrum. Source: Global Warming Art. http://commons.wikimedia.org/wiki/File:Solar_Spectrum.png

2.3. Principle of operation of solar cells

A solar cell can be described as a photosensitive p-n junction or diode. If p-type doped and n-type doped regions of the junction are made of the same semiconductor, the structure is called a homojunction; otherwise it is referred to as a heterojunction. As the result of doping, the p-region has an excess of positively charged holes, while the n-region is rich in negatively charged electrons. Thus, in the p-region, holes are referred to as majority carriers and electrons are called minority carriers while the opposite holds in the n-region. The degree of doping is described by the Fermi level, the maximum energy level that could be occupied by an electron in a semiconductor at temperature of zero Kelvin (0 K). In an intrinsic semiconductor, the Fermi level lies around the middle of the bandgap, in a p-type doped semiconductor it is closer to the valence band, while in the case of an n-type doped material it lies closer to the conduction band.

When the *p* and the *n* parts are brought in contact, excess holes from the p-region start to diffuse into the n-region leaving behind negative ions that are locked in the semiconductor's crystal lattice. Similarly, majority electrons from the n-region start to diffuse into the p-region while leaving behind immobile positive ions. Consequently, an electric field is formed pointing from the positive ions in the n-region toward the negative ions in the p-region and the field opposes the diffusion process. As diffusion continues, this electric field gets stronger and eventually becomes strong enough to stop the diffusion process. At this point the system reaches equilibrium; a potential barrier between the p and n regions, referred to as *built-in* or *diffusion potential*, is formed due to the electric field; the region of immobile uncompensated ions, referred to as the *depletion*

region, is formed at the junction; the conduction and valence energy levels are shifted in such way that Fermi levels of the p-region and the n-region are aligned.

In the equilibrium, majority carriers are prevented by the built-in electric field to pass on to the other side of the junction. On the other hand, minority carriers in close proximity to the depletion region are swept by the electric field over the junction where they are considered majority carriers, but their contribution to the overall concentration of majority carriers is negligible in order to induce a current.

If an external field is applied at the *p* and *n* terminals, it compensates for the built-in field and the system is no longer at equilibrium. In the case of positive bias with respect to the p-terminal (forward bias), the external field is in the opposite direction to the built in field; at a bias smaller than the built-in voltage, the net field is still in the same direction as the built-in field and there is no current flow; at a bias larger than the built-in voltage, the applied field overcomes the built-in field and injects holes from the p-edge of the depletion region into the n-region and electrons from the n-edge of the depletion region into the p-region. The injected carriers continue to flow toward their corresponding electrode and some of them will recombine before reaching the electrode while others will be collected, thus contributing to the current. At this point, the current flow has an exponential dependence on the bias.

If the external field is negative with respect to the p-terminal (reverse bias), the net-field enhances the effect of the built-in field, thus preventing majority carriers from overcoming the junction and swapping minority carriers over the junction more efficiently. As a result, there is a current flow in the reverse direction, almost independent

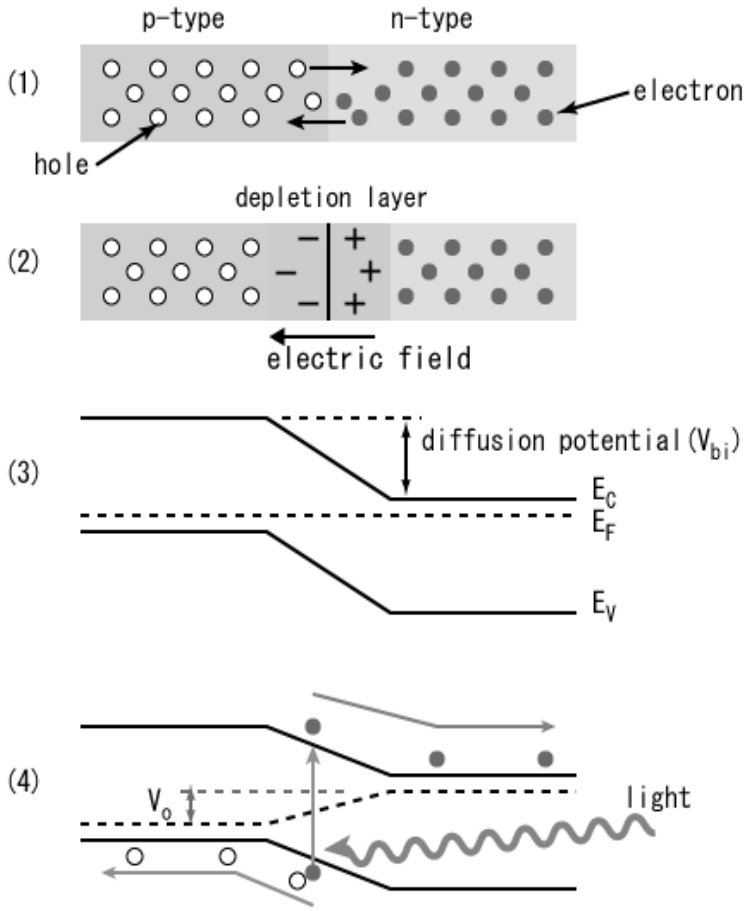

Figure 5. Principle of operation of a solar cell: (1) diffusion process in a p-n junction, (2) thermal equilibrium - formation of the built-in field and depletion region, (3) energy band diagram at thermal equilibrium, (4) photogeneration of electron-hole pairs in depletion region and formation of photocurrent.

of bias and orders of magnitude smaller than in the case of forward bias. Finally, the complete behavior of an ideal diode can be described by the following relation:

$$I = I_0 exp\left(\frac{q(V-V_0)}{nkT} - 1\right) \quad (1)$$

where I is current of the diode, I_0 is reverse saturation current, $V$is applied voltage, V_0 is the built-in voltage, q is the elementary charge, n is diode quality factor, k is Boltzman's constant, and T is absolute temperature.

However, a solar cell is not an ordinary p-n junction; an additional requirement is that it needs to be made of a photosensitive material. When illuminated, generation of free carriers in the depletion region occurs via the photovoltaic mechanism. The generated electrons and holes are separated by the electric field and directed to the n-terminal and the p-terminal, respectively. The concentration of the optically generated carriers is large enough to induce an electrical current, which flows from the n-terminal to the p-terminal. Additionally, the concentration of generated carries is dependent only on characteristics of the incident light, thus not depending on the applied bias. Therefore, the behavior of an idealized solar cell can be described by a slightly modified diode equation

$$I = I_0 exp\left(\frac{q(V-V_0)}{nkT} - 1\right) - I_L \quad (2)$$

where the additional parameter I_L represents the current density generated by incident light. Consequently, the I-V curve of a solar cell is basically a shifted-down version of a diode curve.

2.4. The equivalent circuit model

Based on equation (2), an ideal solar cell can be simply modeled by an ideal current source and an ideal diode connected in parallel. A real solar cell device deviates from an idealized model primarily due to material imperfections and series resistance of the device. Therefore an optimized model of a real solar cell includes two additional components: the shunt resistance, R_{SH}, accounting for material defects and the series resistance of the device, R_S.

The equivalent circuit model is shown on Figure 6. Here, I_L, I_D and I_{SH} represent the photo current, diode current and shunt current, respectively, while V and I represent the output voltage and current, respectively. The output current of the device from the circuit model is $I = I_L - I_D - I_{SH}$. When we substitute the diode expression (1) for I_D into this equation and express I_{SH} in terms of the circuit parameters, we obtain the following expression for the output current:

$$I = I_L - I_0 \left\{ exp\left(\frac{q(V+IR_S)}{nkT}\right) - 1 \right\} - \frac{V+IR_S}{R_{SH}}. \quad (3)$$

I-V characteristics of a solar cell under illumination (I_L> 0) and in the dark (I_L=0) are shown on Figure 7 with solid and dashed lines, respectively. The important parameters determining performance of the cell are the open circuit voltage, V_{OC}, the short circuit current, I_{SC}, and the voltage and current at maximum power operating point, V_{mp} and I_{mp}, respectively.

2.5. Power conversion efficiency

In order to calculate the power conversion efficiency, it is necessary to locate the point of maximum power P_m on the solid line and indentify the corresponding voltage V_{mp} and current I_{mp}. Additionally, the testing conditions of the device are needed. Solar cells are usually tested under standard testing conditions: air mass AM = 1.5, irradiance *E*= 1000 W/m^2, temperature T = 25 °C, and zero wind speed for no cooling effect.[7] Adapting these values, the conversion efficiency can be calculated as

$$\eta(\%) = \frac{P_m}{P_{in}} * 100\% = \frac{V_{mp} I_{mp}}{EA} * 100\% \quad (4)$$

where P_{in} is the input power of incident light, and A is the area of the solar device. In order to maximize the output power it is desirable to increase both V_{OC} and I_{SC} while the shunt resistance should be as high as possible and the series resistance should stay as low as possible. V_{OC} is limited by the bandgap energy of the absorbing material while I_{SC} depends on the absorption and charge transport properties.

The shunt resistance describes the losses of the photo current due to defects introduced into the materials during the fabrication process. The presence of defects introduces so called “traps” or defect states within the bandgap that enhance recombination of free carriers leading to a smaller output current. The current loss due to defects is often referred to as leakage current. The shunt resistance in a solar cell is desired to be as high as possible in order to minimize the leakage current. It can be determined by the slope of tangent line of the I-V curve near the I_{SC} point.

(*a*)

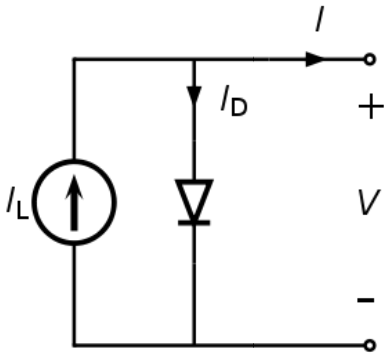

(*b*)

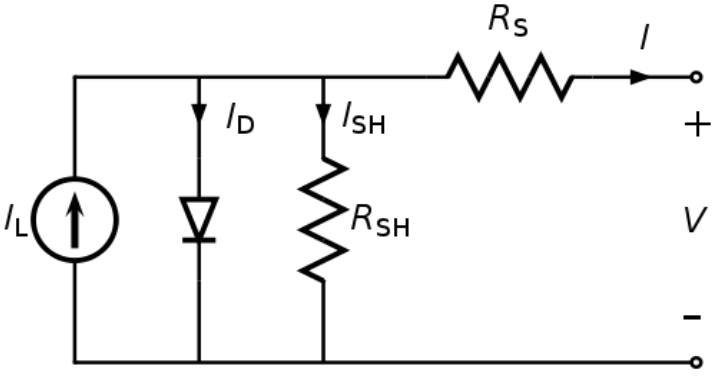

Figure 6. The equivalent circuit of an ideal (*a*) and a real (*b*) solar cell

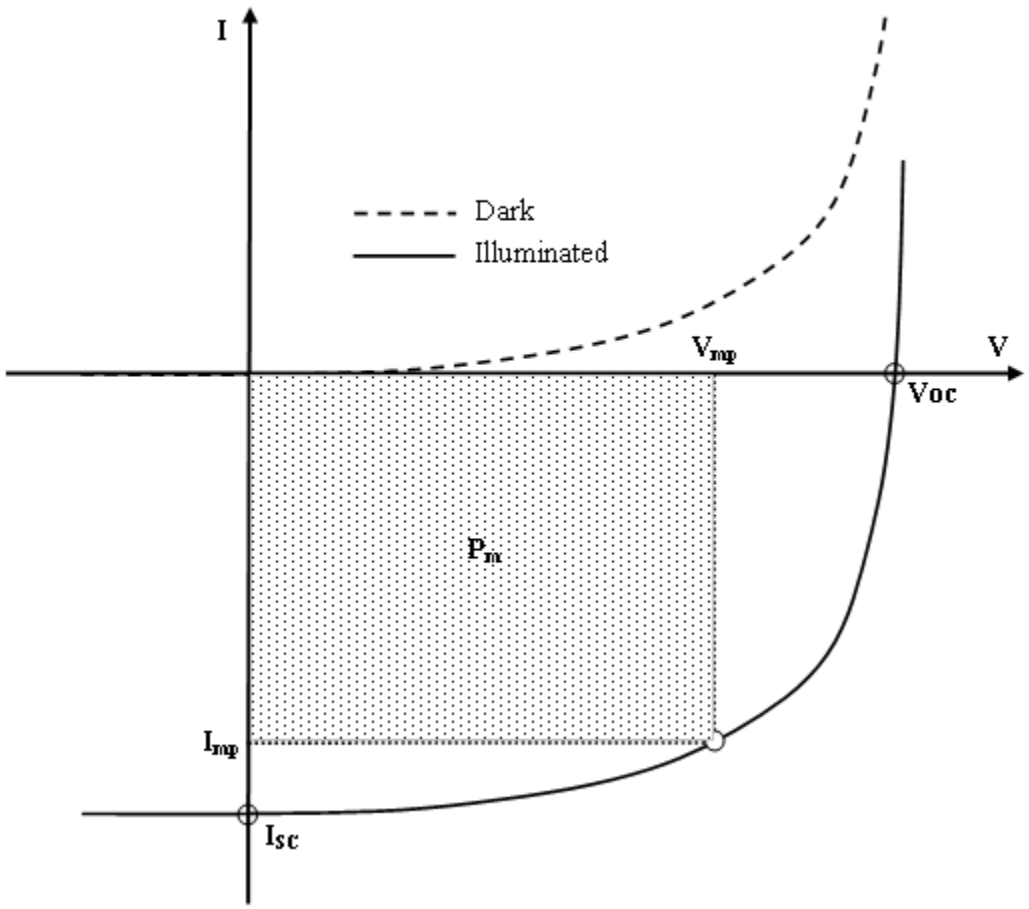

Figure 7. I-V characteristics of a solar cell

The series resistance in a solar cell has three causes: first, the movement of free carriers through the semiconductor; second the contact resistance between semiconductor and metal electrodes; and finally, resistance of the electrodes. The series resistance in a solar cell should be as low as possible in order to maximize power conversion efficiency. It can be calculated as the slope of tangent line of the I-V curve near the V_{OC} point.

An important parameter in the performance analysis of solar cells is fill factor (FF) which measures how close the real device is to the idealized model. An ideal device has infinite shunt resistance and zero series resistance, giving an output voltage equal to V_{OC} and output current equal to I_{SC}, while having fill factor of 100%. Fill factor of a real device has a lower value and can be determined simply as a ratio of the area determined by V_{mp} and I_{mp} and the area defined by V_{OC} and I_{SC}:

$$FF(\%) = \frac{V_{mp}I_{mp}}{V_{OC}I_{SC}} * 100\%. \quad (6)$$

2.6. Heterojunctions

In many cases the *p* and *n* regions of a solar cell junction are made of different materials having differences in electronic properties such as bandgap energy, electron affinity, effective electron and hole masses, etc. Such a junction is called a heterojunction, and a CdTe solar cell is an example of a heterojunction. The principle of operation of a heterojunction device is basically the same as the case of a homojunction device with slight modifications. The band diagram of a heterojunction (Figure 8) can be constructed if the above mentioned parameters are known for each material. First, the conduction

bands are positioned with respect to the vacuum level based on the electron affinity values; second, the valence bands are determined with respect to conduction bands based on the bandgap energies; third, the Fermi levels are estimated for each material based on the doping levels; finally, when the materials are brought together, the Fermi levels align at equilibrium, and as a result, the energy bands bend at the interface.

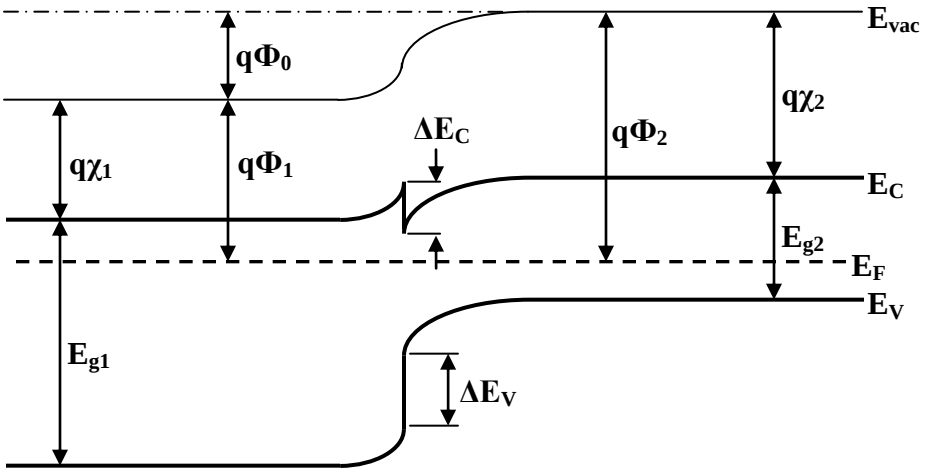

Figure 8. Energy band diagram of a heterojunction

The constructed diagram features two major differences when compared to the corresponding diagram of a homojunction. First, the energy barriers for electrons and holes are not equal, and as a result, the electron injection might be suppressed while the hole injection might be enhanced, or vice versa. The other feature is the energy band offsets at the interface: ΔE_C for conduction band and ΔE_V for the valence band. The

conduction band offset $\Delta E_C = E_{C2} - E_{C1}$ can be negative (Figure 8) and in that case it results in a "spike" in the band diagram at the interface. However the offset might be positive as well and in this case it produces a "cliff" in the diagram at the interface. If the "spike" or the "cliff" is large, it can degrade the photovoltaic performance of the cell. The "spikes" and "cliffs" can be reduced if an abrupt junction is replaced by a graded junction, which is the usual case in real devices due to the interdiffusion of the materials at the interface driven by high temperature of fabrication.

2.7. Semiconductor nanocrystals

As mentioned in the introduction, semiconductor nanocrystals may play an important role in the third generation solar cells with a goal to enhance the efficiencies of photovoltaics. Because nanoengineering is a major concept of this work as well, it is useful to review basic characteristics of nanocrystals before we proceed further.

The simplest version of nanostructures is a quantum well, a one-dimensional structure synthesized of two different semiconductors where the semiconductors of smaller bandgap is a very thin layer sandwiched by layers of the other semiconductor with the larger bandgap. The energy band diagram of a quantum well is shown in Figure 9.

Since the width of the well is of nanoscale dimension, the quantization of energy levels occurs in both the conduction and the valence band. The discrete energy levels for an infinite quantum well can be calculated using a simple formula:

$$E_n = \frac{h^2}{8m^*}\left(\frac{n+1}{L_{QW}}\right)^2 \qquad n = 0,1,2,\ldots \tag{7}$$

where h is Planck's constant, m^* is the effective mass of an electron or hole, n is the quantization number, and L_{QW} is the width of the well. The energy level for n = 0 is called the ground state. The calculation of the discrete energy levels for a finite well is more complicated and requires solution of Schrodinger's equation at the boundaries. However, the infinite well calculation is a good approximation in most cases, especially if energies of the ground states are significantly smaller than the corresponding barriers.

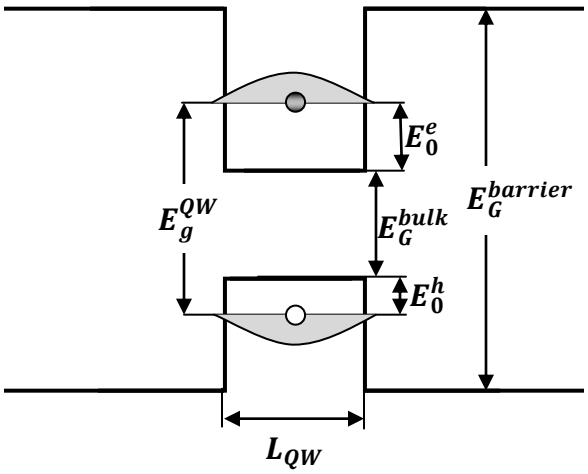

Figure 9. Energy band diagram of a quantum well

Therefore, the effective bandgap of a semiconductor becomes larger as a result of quantization and can be calculated as:

$$E_g^{QW} = E_G^{bulk} + E_0^e + E_0^h \tag{8}$$

where E_G^{bulk} is the badgap energy of the bulk material, and E_0^e and E_0^h are quantized ground state energies of electrons and holes, respectively. The same concept can be extrapolated on quantum dots that are characterized with quantum confinement in three rather than one dimension.

3. POLYCRYSTALLINE THIN FILM CdTe SOLAR CELLS

This chapter describes the fabrication process and function of each layer in the standard cell structure. Additionally, it explores the basic material properties and their effect on device performance and it addresses the main challenges related to the fabrication process.

3.1. Device structure and fabrication process

CdTe cells can be fabricated either in superstrate or substrate configuration. Fabrication in superstrate configuration (Figure 10) starts with a transparent conductive substrate followed with the deposition of subsequent layers and ends with the deposition of a metallic back electrode. The process in the substrate configuration follows the inverse order of deposited layers. Since the best cells fabricated in substrate configuration achieve efficiencies of about 5%, the superstrate configuration is more widely used in fabrication of CdTe devices. Figure 10 shows a basic structure of a standard CdTe solar cell fabricated in superstrate configuration, while Table I outlines the primary processing steps. The devices were fabricated in a matrix of 10 x 10 cells on a single substrate where each device had dimensions of 2 mm x 2 mm.

It is important to mention that cadmium-sulfide (CdS) and CdTe films can be made with a variety of deposition techniques. This fact significantly decreases production costs of the cells. Even though the most common deposition method used is close space sublimation (CSS), CdTe cells have been produced by a variety of other vacuum as well

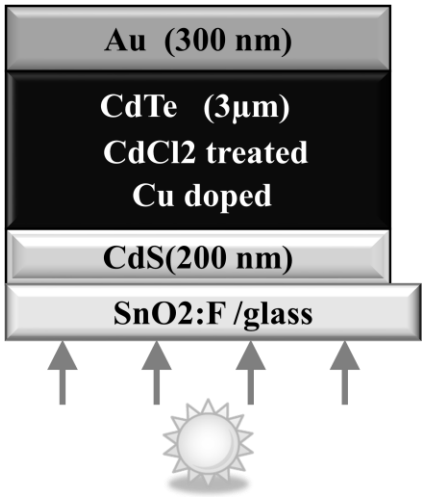

Figure 10. Standard CdTe cell structure in superstrate configuration

Table I Fabrication process summary for a CdTe cell

Layer	Processing step	Comment
Front electrode: SnO_2:F	Piranha clean	-----
Buffer: CdS	Thermal evaporation, 25 °C, 200 nm	Desired temp:150 °C[a]
Absorber: CdTe	RF magnetron sputtering, 150 °C, 3µm	Desired temp:400°C[a]
	Activation treatment: $CdCl_2$ vapor, air flow 0.5 in Hg, 425 °C, 20-30min	Home-built setup
Back contact: CdTe/Au	Br/CH_3OH doping: 3% aqueous solution, 12 sec	-----
	Cu doping: e-beam deposition (25Å); post annealing 180°C, 15 min	-----
Back electrode: Au	e-beam deposition, 300 nm	-----

[a] Deposition temperatures were limited by the laboratory policy

as non vacuum techniques. Vacuum techniques include thermal and e-beam evaporation, atomic layer deposition (ALD), and metal organic chemical vapor deposition (MOCVD), while the most common nonvacuum techniques are electro-deposition, chemical bath deposition (CBD), screen printing, and solution spray.

3.1.1. The front contact: SnO_2:F

The purpose of the front contact in the cell structure is to transmit incident light into the absorber and to form an electrode for the collection of photo-generated carriers. Therefore, it needs to be a transparent and a conductive material and the thickness of this layer is constrained by the trade-off between transparency and conductance. The most common choices for this purpose are transparent conductive oxides (TCO) including indium doped and fluorine doped tin-oxide. Additionally, the front contact provides mechanical strength in the superstrate configuration. In this work, fluorine-doped tin-oxide (SnO_2:F) was used as the front electrode. The bandgap of this material is around 3.7 eV.[8]

3.1.2. The buffer layer: CdS

The purpose of the buffer layer in the cell structure is to form the n-region of the p-n junction. The choice of the buffer layer is constrained by the optical and electrical characteristics of the material as well as compatibility with the fabrication process. CdS turns out to be the best available partner to CdTe for a number of reasons.

Since the buffer should transmit a maximum amount of the light into the active layer where the light should be absorbed, optical absorption in the buffer should be avoided. This condition limits the choices to wide bandgap materials. Also, from this point of view, the buffer layer needs to be as thin as possible but it should not be completely depleted. CdS has a bandgap of 2.42 eV[9] at room temperature, which is almost 1 eV higher than the bandgap of the absorber, CdTe, while its typical thickness is a few tenths of a micron.

The energy band offset between the buffer and the active layer should not be significant. At first approximation, the offset is simply calculated as the difference in electron affinities χ of the materials forming an interface. If the level of the conduction band of CdTe is sufficiently above the level of the conduction band of CdS, a "cliff" in the band diagram appears at the interface, which results in loss of open circuit voltage V_{OC}. In the case of sufficiently higher conduction band level of CdS with respect to the conduction band of CdTe, a "spike" in the band diagram appears at the interface, which decreases the short circuit current I_{sc}. The estimated offset at the interface between CdS and CdTe predicts formation of an allowable small "cliff" of 0.22 eV[9] in the band diagram.

The lattice mismatch between an absorber and a buffer layer should be small in order to minimize the strain and the number of interface states. The mismatch between CdS and CdTe is relatively large inducing a significant number of surface states. However, the intermixing between CdTe and CdS occurring at the higher deposition temperatures of CdTe promotes a smoother transition between the lattices and thus relaxes the strain between the materials, resulting in decent performance of the junction.[9]

Additionally, the buffer layer should be compact in order to avoid shunt resistance between the absorber and the front contact. Finally, the crystallographic structure of the buffer influences the morphology of the absorber since it serves as an under-layer for the growth of the absorber. For the last reason, the buffer layer should not be too thin.

3.1.3. The active layer: CdTe

The CdTe layer, the active layer or the absorber, is responsible for the main photovoltaic conversion in the cell. It has optimal optical and decent electrical properties for this purpose. Its direct bandgap of around 1.45 eV is in the optimal range for maximum photovoltaic conversion while its high optical absorption coefficient allows absorption of most of the incident light by a film only 2-3 μm thick. The minority carrier diffusion

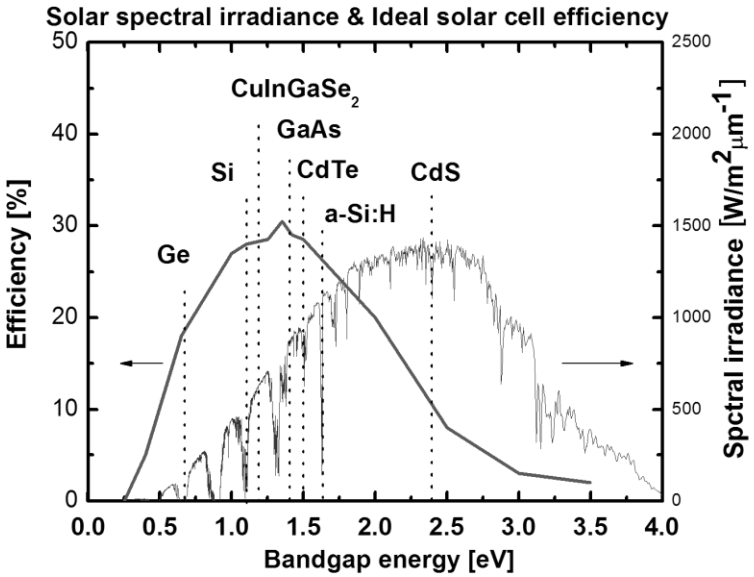

Figure 11. Solar spectral irradiance and ideal solar cell efficiency for common inorganic materials. Source: The United States Department of Energy, http://www.nrel.gov/rredc/

length is about 1 μm, which allows a majority of generated carriers in a thin film to be collected at contacts.

One of the electrical properties of CdTe that is negative is the fact that it is difficult to control the doping density and achieve a high p-type doping due to native defects. Also, many of the chemical elements associated with the fabrication process introduce impurities in CdTe. It is known that group I elements and group V elements, replacing Cd and Te respectively, act as shallow acceptors, while group III and group IV elements, substituting Cd and Te respectively, act as shallow donors.[10-11] On the other hand, isoelectric elements, such as Zn, replacing Cd, and S or Se substituting Te, do not introduce defect states.[11] Other impurity elements usually act either as deep acceptor or deep donor states.[12] In conclusion, the recombination properties of CdTe depend on the preparation method. However, the activation treatment compensates most of these effects resulting in decent performance of the device.

The grain size in polycrystalline thin films depends on deposition technique. In general, larger grain size is preferred since generated carriers have to overcome fewer grain boundaries thus having a better chance to be collected. Following this logic, one can assume that the best performance of these devices could be achieved if single crystal films replace polycrystalline films.

However, polycrystalline CdTe cells show better performance compared to their single-crystal counterparts. This phenomenon can be explained by the distortions of the band diagram around grain boundaries due to charged interface states, doping gradient in the interior of the grains near grain boundaries, diffusion of impurities or their segregation at

the grain boundaries, and material modifications at the boundaries.[9] If the band diagram at the grain boundary features a potential barrier for electrons and accumulation for the holes, it is beneficial for photovoltaic operation since it enhances the hole conduction and reduces electron recombination; on the other hand, a barrier for holes and accumulation of electrons at the site of a grain boundary would enhance recombination at the boundary and thus have an unfavorable effect; the third scenario, embedding both a barrier for electrons and a barrier for holes (double barrier) with an accumulation of holes at the boundary, passivates the boundary and thus has a positive effect on photovoltaic conversion. In conclusion, polycrystalline films are preferred, but with larger grain size.

Doping and recombination properties of the CdTe layer usually depend on deposition technology, but after the activation treatment it features p-type doping even though high doping levels are not easily achieveable.[9] It is very difficult or even impossible to measure properties of CdTe on a fabricated cell due to material interactions and intermixing between CdTe and other layers in the cell structure, which are driven by relatively high temperature fabrication processes.

3.1.4. Activation of the junction: $CdCl_2$ treatment

The activation treatment with $CdCl_2$ is an unavoidable step in fabrication of CdTe solar cells. Without this treatment, the maximum achievable conversion efficiency of these devices would be an order of magnitude smaller.[13] $CdCl_2$ treatment is usually performed by applying a thin film of $CdCl_2$ on the CdTe layer via CSS evaporation, followed by an annealing treatment at temperatures above 400 °C. Chemical reactions of chlorine (Cl_2) along with influences of the annealing temperatures usually result in passivation of

native, impurity and interfacial defects, thus improving electrical properties of Cd-containing layers. An alternative version is treatment with $CdCl_2$ vapor also at higher temperatures, which has been used in this work. A schematic diagram of our home-built setup is shown in Figure 12.

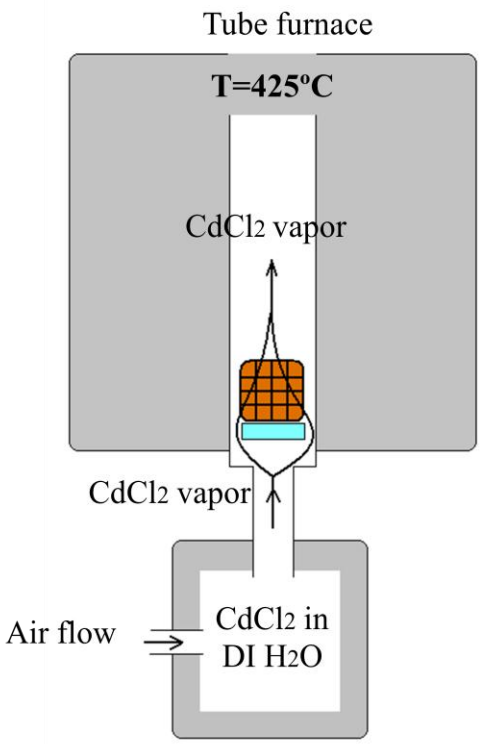

Figure 12. Home-built setup for $CdCl_2$ treatment

Firstly, the $CdCl_2$ treatment affects morphology of CdTe. It improves internal crystallographic structure of grains and promotes the grain growth if the initial size of grain was small. Secondly, it affects the doping and recombination properties of CdTe. The p-type doping of CdTe is established or enhanced and n-type doping of CdS might be enhanced. Passivation of deep electronic states occurs in the bulk or at the interface

but introduction of some other deep states might occur as well. An overtreatment can induce a large population of deep electronic states resulting in loss of V_{OC} or can cause adhesion issues. Finally, $CdCl_2$ treatment promotes intermixing at CdS/CdTe interface, thus reducing the "cliff" in the band diagram.[9]

3.1.5. Optimization of the back contact

In order to efficiently collect generated charge carriers, the energy band diagram at the contact between the semiconductor and its metal electrode should not have a significant barrier. In our case we need to suppress the energy barrier for holes at the interface of CdTe with the back Au electrode. The back contact not only needs to be of low resistance but has to be stable as well.

The main problem in finding an ohmic and stable contact to the CdTe is due to the difficulty in achieving a high doping density of CdTe. As a result, CdTe requires a metal with very high electron affinity in order to decrease the barrier at the back contact. The only metals featuring this property are noble metals, which is not a favorable choice from the economic perspective.

One of the more successful approaches to optimize the back contact is the enhancement of p-type doping of the CdTe surface with copper (Cu).[14] This approach gives good results initially but it is not stable in the long run due to the fast diffusion of Cu in CdTe material;[15] if copper concentration is sufficiently high, Cu atoms diffuse over time toward the p-n junction and eventually reach and even pass the junction penetrating into the CdS region, which results in degradation of the device.

Another approach to achieve high doping density of the CdTe surface is to etch it in bromine-methanol solution. This way, Cd atoms are etched away from the surface leaving a Te-rich surface.[16] Since an increase in Cd vacancies at the surface forms shallow acceptors, the etching enhances the p-type doping at the surface. In this work, a combination of the bromine/methanol etching approach and copper doping was used.

Finally, a Au film was evaporated on the CdTe and annealed in order to form the back electrode. Au contact is an optimal choice due to the trade-off between high electron affinity and cost.

3.2. The energy band diagram

From the previous discussion, it is possible to construct a hypothetical band diagram at equilibrium of a fabricated cell. The major material parameters for Cd compounds are listed in Table II. Here, an assumption is made that the CdS layer is uniformly n-type doped at a moderate level. Another assumption is that intermixing of CdS and CdTe at the junction happens over a smaller distance (e.g. 100 nm). Since p-type doping of CdTe occurs during $CdCl_2$ treatment from the back contact interface, a reasonable assumption is that CdTe has a linear doping profile; it is assumed that CdTe exhibits a near-intrinsic characteristic at the CdS/CdTe interface with an increasing p-type trend moving towards the back contact. Additionally, significantly stronger p-type doping is expected at the back contact due to the bromine-methanol etch and Cu doping. The effect of material defects is neglected for simplicity in this case. The resulting diagram is shown in Figure 13.

Table II Some basic electrical properties of common Cd compounds

Property	Symbol	Unit	CdTe[9]	CdS[9]	CdSe
Bandgap (300k)	E_g	eV	1.45	2.42	1.71[17]
Electron affinity	χ	eV	4.38	4.50	4.95[17]
Electron effective mass (relative)	m_e^*	---	0.10	0.20	0.13[18]
Hole effective mass (relative)	m_h^*	---	0.40	0.80	0.45[18]

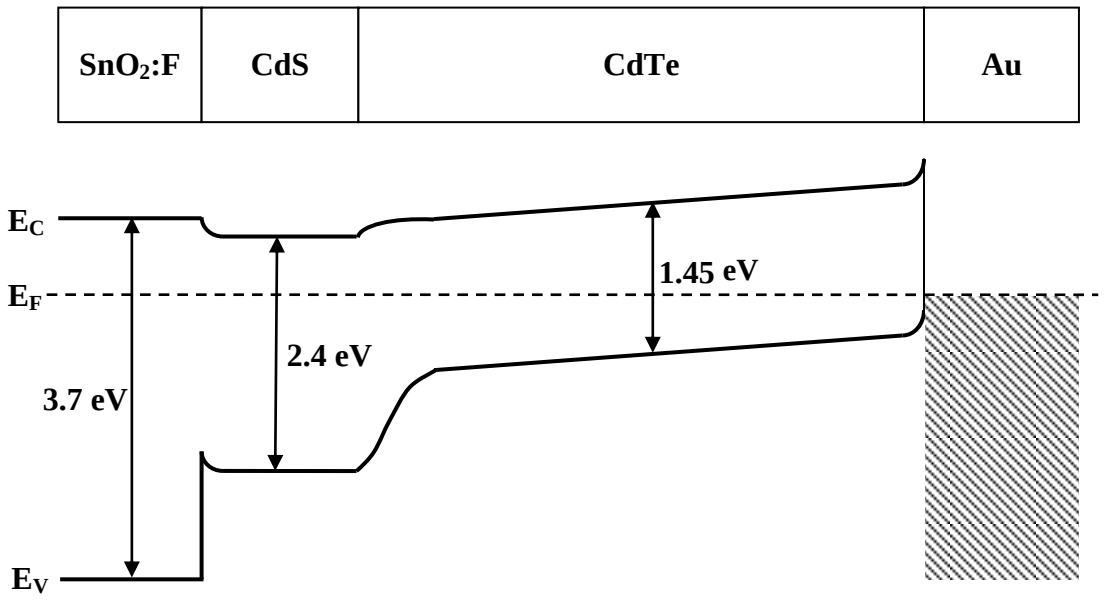

Figure 13. Energy band diagram of a CdTe cell

3.3. Testing

The fabricated devices were tested on our home-built setup. The setup consists of a light source calibrated to irradiance output of 0.1 W/cm^2, an automated I-V setup, and a sample stage. The measurements for each device were performed at room temperature in the dark and under illumination. The data were acquired automatically in the voltage range from -0.5 V to 1 V. The I-V curves obtained are discussed in detail in the following chapter.

4. EFFICIENCY ENHACEMENT OF CdTe SOLAR CELLS VIA NANOENGINEERING

First, this chapter gives an overview of theoretical limits for single junction solar cells. Second, it analyzes primary losses in solar cells and identifies approaches for efficiency improvements. Then, advanced theoretical models for the efficiency enhancement are proposed. This is followed by description of the fabricated device structures with a nanocrystalline layer inserted, which implements some of the proposed ideas. After this, the experimental results are presented. Finally, the chapter ends with a summary of the results and conclusions.

4.1. Theoretical efficiency limits

The maximum obtainable power conversion efficiency for a single threshold absorber was calculated by Shockley and Queisser in 1961.[19] The upper efficiency limit of such material, known as the Shockley-Queisser limit, is about 30% at 1 sun and can achieve about 40% under concentrated sunlight. This calculation assumed an idealized device so the practical limits are even smaller. The main assumptions are that all incident photons are captured, all above-band-gap photons are absorbed, complete thermalization occurs, the transport and collection of charges are lossless, and that only radiative or Auger recombination occurs. Applying the same concept to CdTe solar cells, the estimated upper limit reaches about 30% efficiency, which is almost double of the current highest efficiency achieved.

4.2. Practical efficiency limits

It is important to identify primary losses in a photovoltaic conversion in order to identify the best approaches for efficiency improvements. These losses could be either due to a non optimized utilization of the solar spectrum or due to imperfections of the materials. A significant minimization of the primary losses could lead to a direct enhancement of the conversion efficiency.

There are four major kinds of losses during photovoltaic conversion in a solar device (Figure 14). First, sub-bandgap photons cannot be absorbed and thus their energy is not utilized. On the other hand, the photons with energy that well exceed the bandgap energy of the absorber participate in the conversion process only with a portion of their energy, which is equal to the bandgap energy; the high energy photons generate hot carriers that relax to the conduction band minimum and the valence band maximum before they are collected at electrodes; thus, the extra energy of hot carriers is wasted as heat through phonon emissions. A choice of the bandgap energy for optimal solar spectrum utilization is accompanied with a trade-off between the sub-bandgap and hot carrier losses and thus it does not imply a significant improvement of the device.

The third kind of loss is recombination via electronic states within the bandgap. Intermediate traps are produced by native defects and impurities in the material. Minimization of these losses involves morphological improvements of the materials and is not an objective of this work.

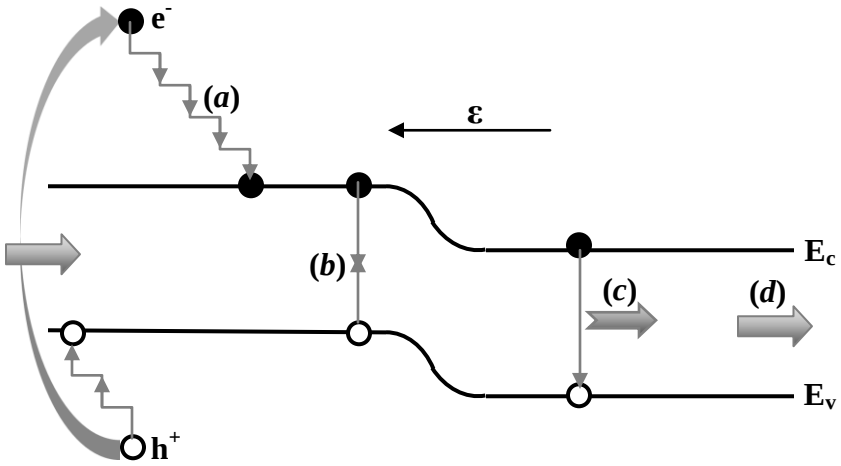

Figure 14. Primary losses in a solar cell:
(*a*) Sub-bandgap photons are not absorbed.
(*b*) Hot carriers relax to the conduction band minimum and valence band maximum by emitting phonons; thus the excess energy is wasted as heat.
(*c*) Recombination of carriers through the traps within the bandgap
(d) Radiative recombination of excitons which results in emission of photon of the near bandgap energy;

The fourth kind of loss is radiative recombination of electron-hole pairs, which results in emission of photons at the bandgap energy. Some of the generated photons are reabsorbed and may contribute to the conversion efficiency. However, some of the photons are not reabsorbed, especially those that are emitted backwards to the front contact and do not contribute to the photocurrent.

4.3. Mechanisms for efficiency enhancement

4.3.1. Intermediate-Band concept

Sub-bandgap photons can be utilized if a narrow density of states, referred to as the intermediate band (IB), exists within the bandgap. Besides the ordinary absorption process between the valence band and the conduction band, there are two additional allowed transitions in this case – between the valence band and the IB, and between the IB and the conduction band. The last two transitions utilize the sub-bandgap photons, which should improve the conversion efficiency of the device.

The IB can be realized by introducing a nanostructured layer into the junction. The layer can be composed of periodic, closely packed quantum dots with an effective bandgap significantly smaller than the bandgap of the absorber. In an ideal case, quantum confinement, periodicity and close proximity of the nanocrystals lead to formation of mini-bands and multiple quasi-Fermi levels within the bandgap of the absorber. Unfortunately, the experimental work on IB cells performed to date resulted in reduced efficiencies due to lower open circuit voltages, even though the sub-bandgap response has been detected.[20]

4.3.2. Plasmonic effect

Nanoparticles of noble metals demonstrating enhanced absorption bands in the visible and ultraviolet region of the spectrum[21] can be applied at the front contact of a solar cell in order to improve its efficiency. The incident light causes oscillations of conduction electrons in the metallic nanostructures.

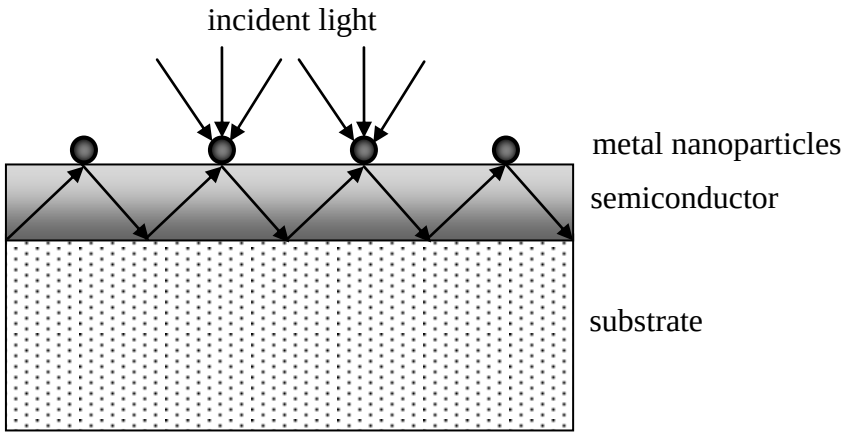

Figure 15. Plasmonic solar cell

When photons interact with the metal nanoparticles oscillating at their surface plasmonic resonance, the absorption enhancement may be promoted resulting in higher external quantum efficiency. Additionally, unabsorbed light scatters and travels along the absorbing layer in all different directions, bouncing back and forth between the substrate and the nanocrystalline layer until it is finally absorbed. This concept is illustrated in Figure 15.

4.3.3. Multiple exciton generation

The high energy photons of the solar spectrum can be more efficiently exploited using the concept of impact ionization. In this process, the high energy of a photon is absorbed by an electron and thus converted into a high kinetic energy of the electron. Due to its high kinetic energy, this electron is able to knock out an additional electron from the valence band via a collision process. The original electron is scattered with a reduced energy but it is still in the conduction band, while the knocked electron is excited to the conduction band. Thus, additional excitons are generated from the original photon and quantum yield

is increased. The main requirement for the process to occur is that the photon energy is at least twice the bandgap energy. This concept can be extended to generation of multiple excitons for a photon, where the photon energy is multiple times greater than the bandgap energy, even though the probability for such events is extremely low.

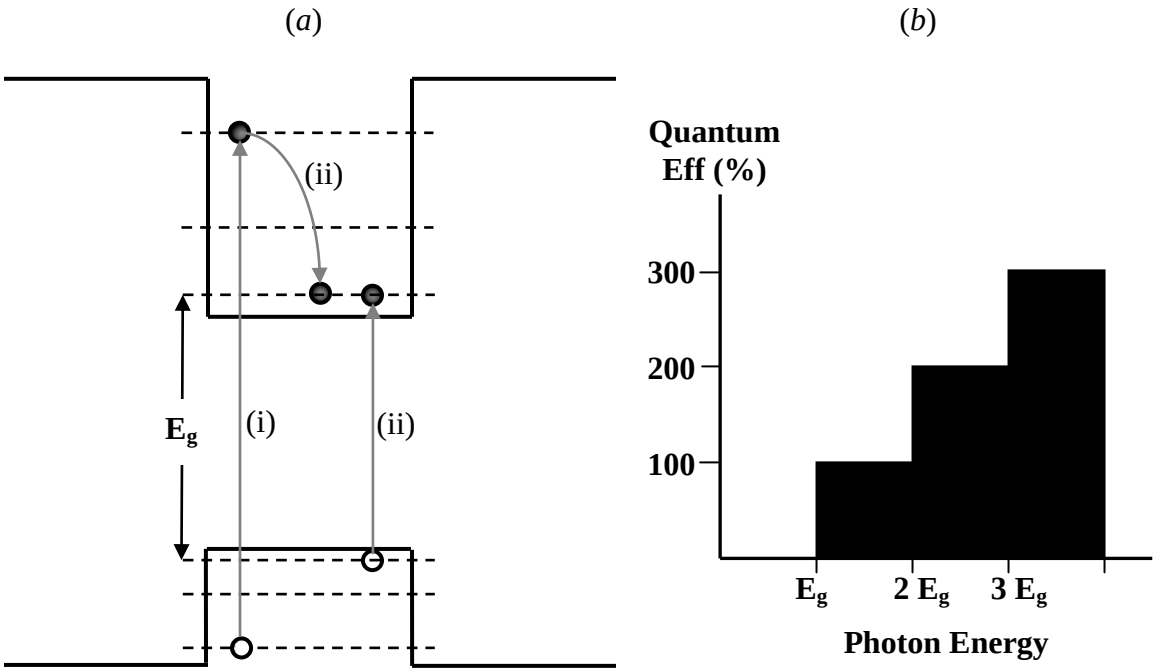

Figure 16. MEG process:
(*a*) Energy-band diagram representation
(*b*) Quantum efficiency as a function of the photon energy

MEG in semiconductor materials competes with other processes present such as phonon scattering, inelastic carrier-carrier scattering, Auger recombination, and exciton-exciton annihilation. In bulk materials phonon scattering rates are significant and MEG is not likely to occur unless the photon energies are extremely high. However, MEG may be greatly enhanced in quantum dots due to quantum confinement, increased electron-hole

Coulomb interactions and no necessity for conservation of crystal momentum. As a result, a very efficient MEG process in PbSe, PbS, PbTe, and CdSe quantum dots has been reported.[22]

4.3.4. Photon energy conversion

Another approach to improve solar cell efficiencies is to convert the polychromatic solar spectrum to a spectrum optimized for a solar cell. Multiple sub-bandgap photons can be converted into an above-bandgap photon through subsequent absorptions (up-conversion). Similarly, a high-energy photon can be converted into multiple above-bandgap photons through subsequent radiation (down-conversion).

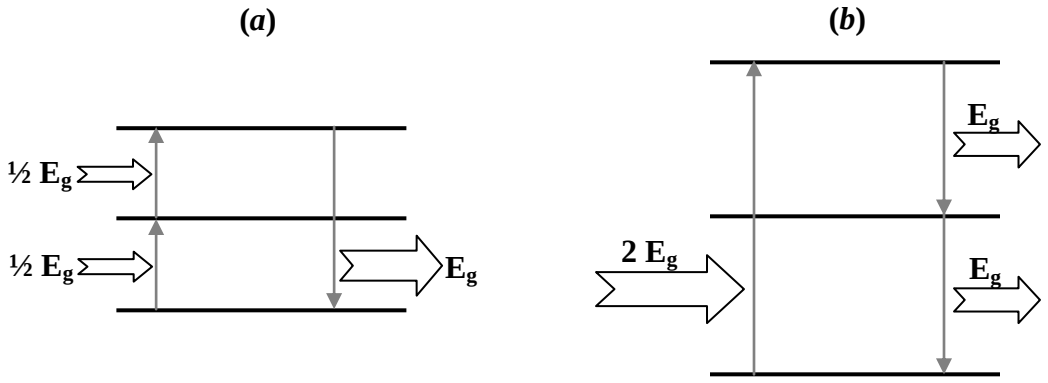

Figure 17. Photon energy conversion:
(*a*) up-conversion
(*b*) down-conversion

4.3.5. Fluorescence resonant energy transfer

FRET is a nonradiative transfer of energy from a donor particle to an acceptor particle. The transfer of energy does not involve emission and reabsorption of photons, particle collisions or heat transfer, but it is caused by dipole-dipole interactions between electronic states of the donor and the acceptor. The process can be simply explained by a virtual photon emitted by the donor and instantly absorbed by the acceptor. The strength of the interaction depends on the overlap of the fluorescence emission spectrum of the donor and the absorption spectrum of the acceptor as well as on the magnitude of the dipole interaction and the alignment and separation of the dipoles.

4.4. Fabricated device structures

Three types of device structures were fabricated in this study: the standard CdTe solar cells that were used as control cells referred to as "structure *a"* devices (Figure 18 a); CdTe cells with a nanocrystalline layer inserted between CdS and CdTe layers, referred to as "structure *b*" devices (Figure 18 b); and CdTe cells with a nanocrystalline layer inserted in between the front contact and CdS layers, referred to as "structure *c*" devices (Figure 18 c). The structures with nanocrystalline layers were fabricated using the same procedure as in the case of the control devices, outlined in Table I; the only difference is the additional nanocrystalline layer, which consists of colloidal quantum dots (QDs) applied by the drop-casting technique.

Additionally, both structures *b* and *c* were fabricated in three variations: with Au, CdSe, and CdS QDs. The choice of the QDs was subject to availability. Gold QDs in both

structures *b* and *c* were used to demonstrate the plasmonic effect in CdTe cells. The CdSe and CdS QDs were used to promote the MEG process but they might provide the photon energy down-conversion process or even FRET effect.

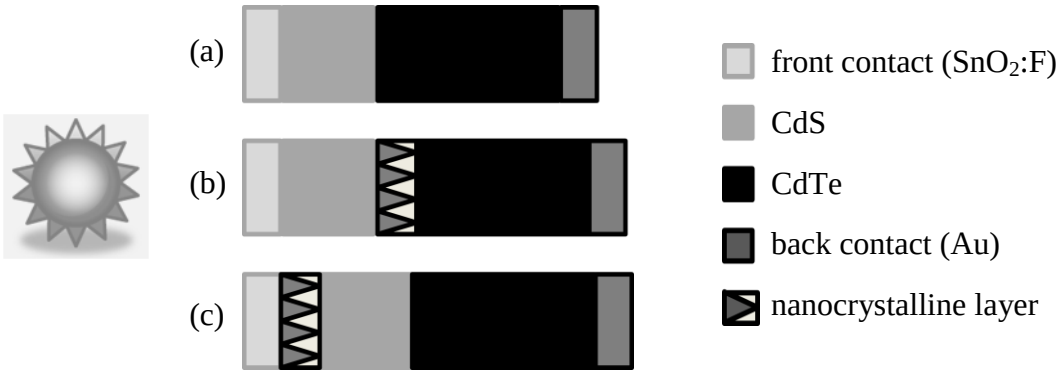

Figure 18. Fabricated device structures:
(a) Standard cell (control device)
(b) Nanocrystalline layer inserted between CdS and CdTe layer
(c) Nanocrystalline layer inserted between the front contact and CdS layer

CdSe QDs employed for MEG process are not capable of a significant efficiency enhancement because only photons with energies greater than 4 eV, accounting for a fraction of a percent of the solar spectrum, can be utilized. In case of CdSe QDs used in the spectrum down-conversion process, the potential for the improvement is somewhat better since photons of energies above 3.5 eV can be utilized and they account for about 5% of the solar spectrum. Compared to CdSe QDs, CdS QDs are less capable of enhancing the efficiency through these processes because of their larger effective bandgap energy.

Au QDs used in this work were colloidal QDs in toluene with size of about 10 nm and of light violet color, purchased from Sigma Aldrich. The CdS QD were also colloidal dots, yellow in appearance, and were synthesized in house by previous group members. The CdSe dots were also in house synthesized colloidal QDs, orange in appearance.

4.5. Experimental results

The device structures from Figure 18 were fabricated following the previously described procedures. Fabrication of the structures with nanocrystalline layer, *b* and *c* in Figure 18, proved difficult due to adhesion issues, while the structure *a* was as expected. In order to identify the primary reason for the adhesion problems, the nanocrystalline layer was examined more closely.

4.5.1. Effect of annealing treatment on quantum dots

Photoluminescence data

First of all, emission spectra of the QDs were collected by photoluminescence (PL) measurements. For this purpose, the dots were assembled on glass substrates. As shown in Figure 19, Au dots feature two peaks at about 455 nm and 505 nm, suggesting two different sizes of the dots in the mixture. Unfortunately, the CdS dots didn't feature any PL peaks in the expected range suggesting degradation in materials properties. Finally, the CdSe QDs showed a strong PL peak around 585 nm which corresponds to the effective bandgap energy of about 2.1 eV.

Further, the assembled dots were annealed at 425 °C for 30 min in order to examine their behavior after exposure to temperatures that are utilized for the $CdCl_2$ treatment. The PL measurements of the annealed quantum dots showed an absence of any peak suggesting degradation of the material properties under the exposed temperature.

Optical microscopy data

Additionally, the QDs were examined with an optical microscope before and after the annealing treatment (Figure 20). Before the annealing treatment, the microscope images revealed a significant population of Au clusters of size of about 1 μm in diameter. Additionally, a large population of CdS clusters had the same size while a smaller population of the clusters had a size of about 10 μm. Finally, the images of the CdSe QDs did not reveal any particles on a micron scale.

The images of the QDs after the annealing treatment are shown at the bottom part of Figure 20. Au clusters merged together at the high temperature and formed much larger clusters. Some of these broke and peeled off the substrate leaving behind large pinholes in the film. Similar behavior was seen in the case of the CdS dots except that the pinholes formed were somewhat smaller. The CdSe QDs experienced even more severe degradation due to the annealing treatment. The behavior of the dots under annealing might be somewhat different when they are inserted in the cell structures *a* and *b*, but this experiment points out the incompatibility of the drop-cast nanocrystalline layer with the standard fabrication procedure of CdTe solar cells.

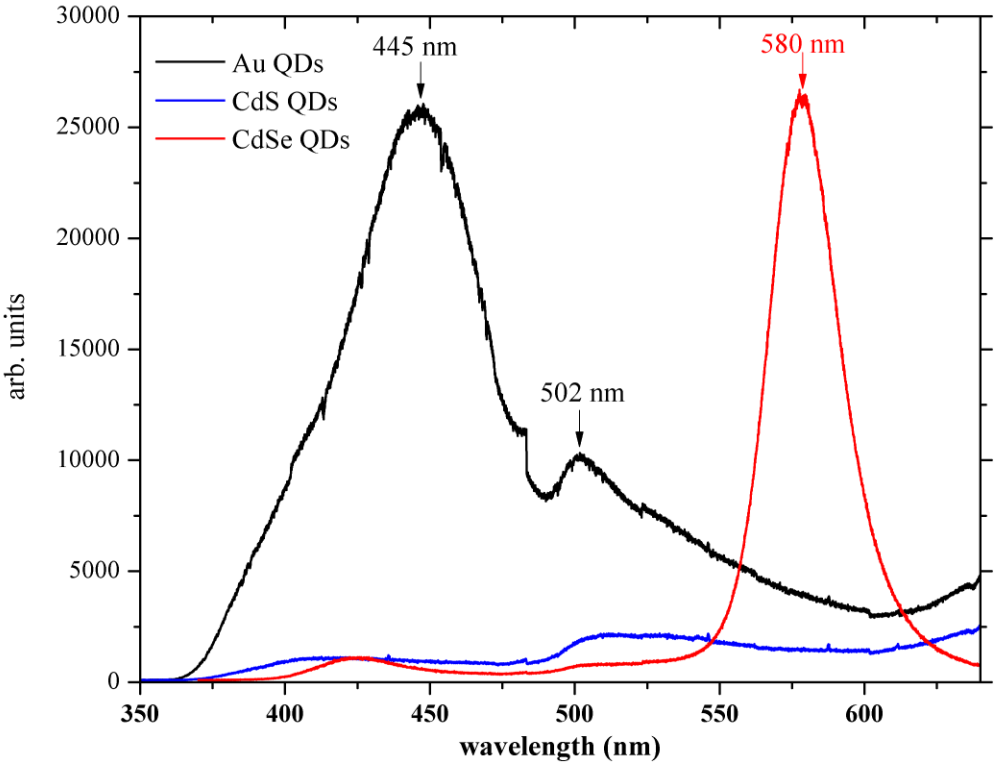

Figure 19. PL spectra of Au, CdS, and CdSe quantum dots before annealing treatment. The excitation wavelengths: 325 nm. The PL peaks disappear after annealing.

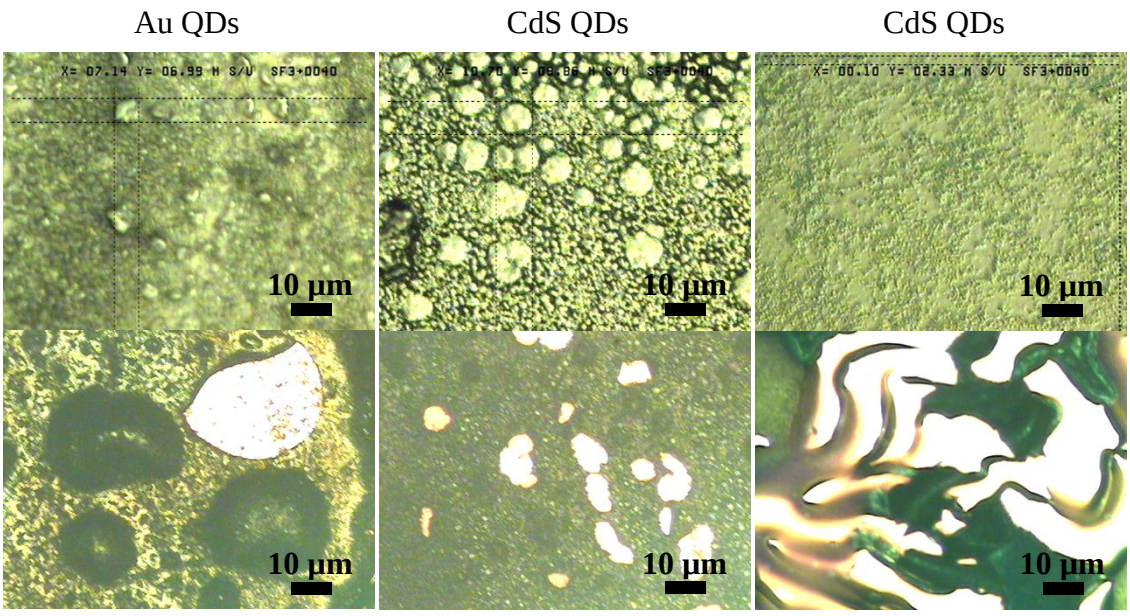

Figure 20. Microscope images of Au, CdS, and CdSe quantum dots on glass substrate before (top) and after (bottom) annealing treatment at 425 °C for 30 min

4.5.2. Effect of the $CdCl_2$ treatment

The tremendous influence of $CdCl_2$ treatment on performance of CdTe cells was discussed in detail in Chapter 3. Also, our home built setup is described in the same section. The home built setup was not optimized and led to nonuniformities and lack of control over the fabricated cells. Additionally, those devices with a nanocrystalline layer suffered from lack of adhesion in most cases. However, it is still possible to make some conclusions regarding the effect of $CdCl_2$ treatment on the fabricated cells.

The duration of the $CdCl_2$ treatment was also varied, 30 min versus 20 min, for each type of device structure, while the annealing temperature was kept constant at 425 °C. Conclusions regarding the influence of the treatment on cell performance are drawn from the comparison of the I-V curves corresponding to each of the fabricated structures.

First of all, it is important to address the imperfections of our setup for $CdCl_2$ treatment. Due to nonuniformity of the vapor flow over a substrate containing a matrix of 10 x 10 cells, all cells are not equally exposed to the treatment. The substrate with the cells was protected from direct flow of $CdCl_2$ vapor by a glass barrier so the vapor travelled sideways only (Figure 12) but it reached various regions of the substrate at different speeds. As a result, the spatial distribution of the cell efficiency on the substrate has a radial-like shape.

Effects of nonuniformity of $CdCl_2$ treatment are the most obvious in the case of control devices treated for 30 min. Figure 21 *a* shows a substrate with a hundred such cells. All tested devices can be divided into four regions with respect to the measured power conversion efficiency: 0 - 0.5 %, 0.5 - 1.0 %, 1.0 - 1.5 %, and 1.5 – 2.3 %. Devices

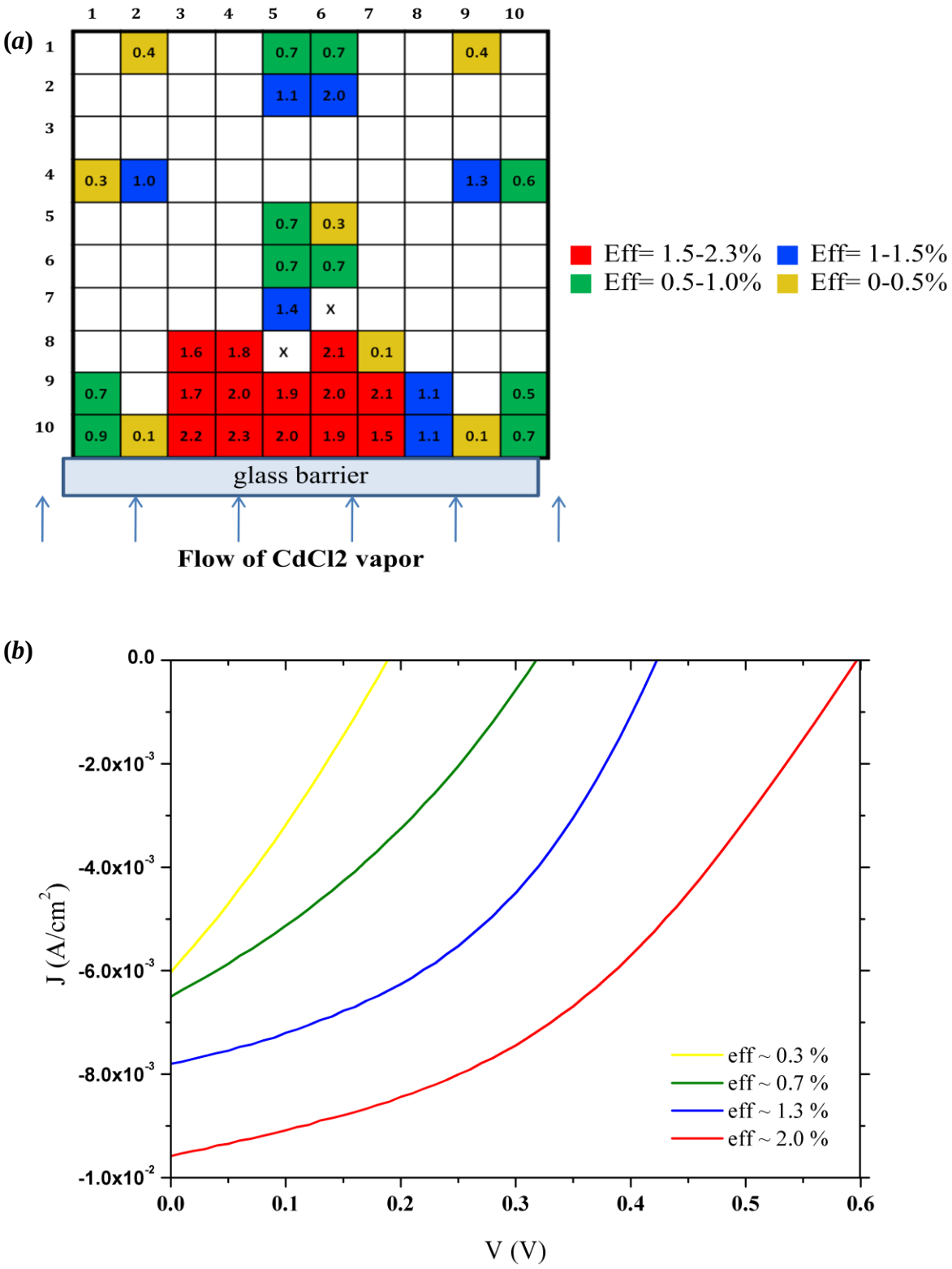

Figure 21. Control devices: (*a*) spatial distribution of efficiencies on a substrate with 10 x 10 cells as an effect of nonuniform $CdCl_2$ treatment; (*b*) I-V curves of the representative cells from each of the four regions.

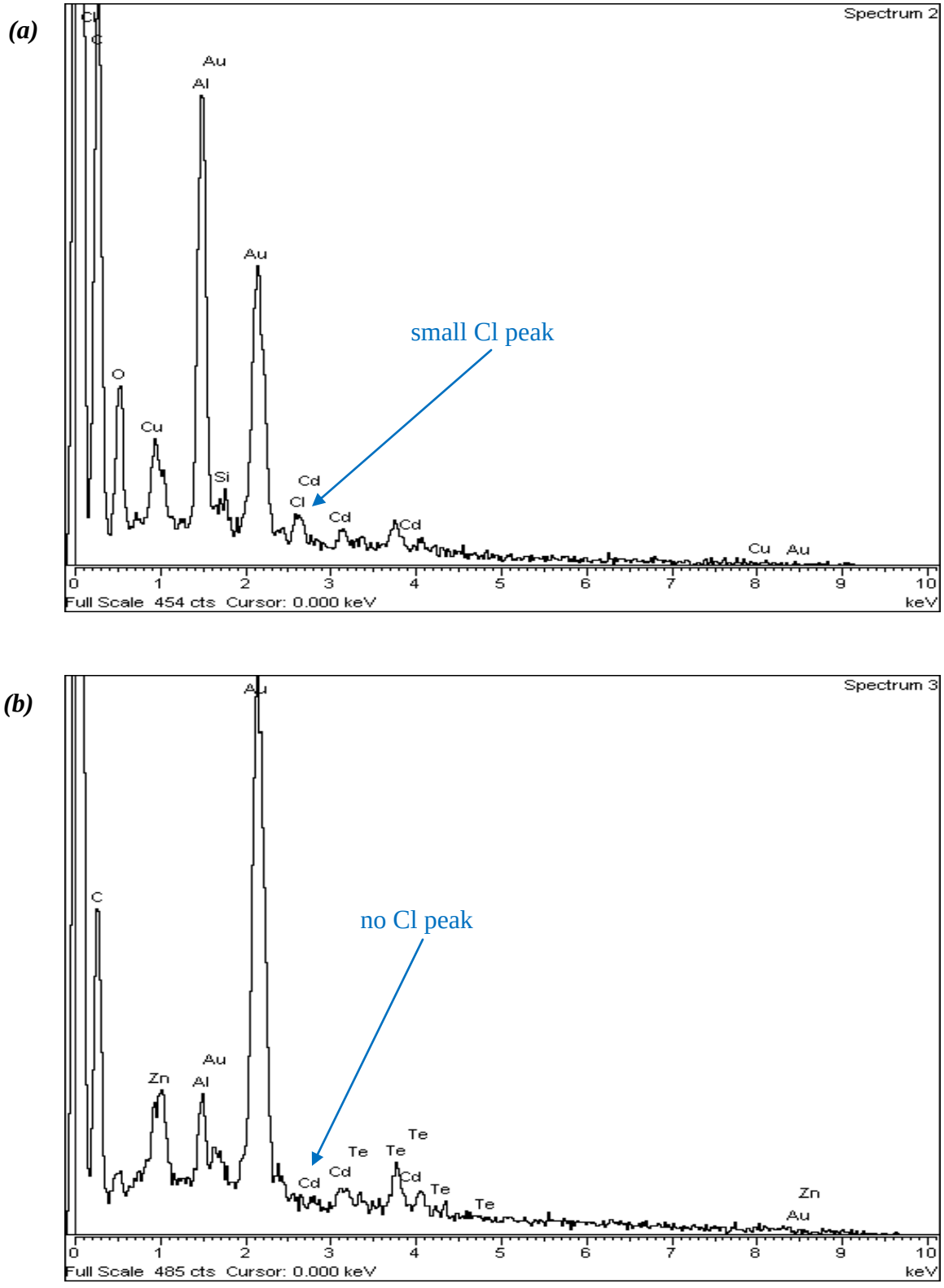

Figure 22. EDX spectra of CdTe film at the region of the substrate with higher efficiency (*a*) and at the region of the substrate with lower efficiency (*b*). Weak Cl peak (*a*) and absence of Cl peak (*b*) indicate $CdCl_2$ undertreatement.

in the best efficiency range, 1.5 – 2.3 % marked with the red pattern, are located in the middle of the frontal region of the substrate, right behind the glass barriers (Figure 21 *a*).

Figure 21 *b* illustrates the I-V characteristics of the representative devices from each of the four efficiency ranges. It is interesting to note that both V_{oc} and J_{sc} are decreasing as the efficiency decreases. This is due to unequal passivation of defects and other recombination centers caused by nonuniform exposure to $CdCl_2$ vapor. The decreasing trend of the efficiency in Figure 21 *b* can be due to either an undertreatment or an overtreatment with $CdCl_2$ vapor. However, Figure 22 showing the EDX spectra measured at the red (*a*) and yellow (*b*) region respectively, indicate a low concentration of Cl at the red region, while there is no Cl peak at the yellow region. This is an indication of $CdCl_2$ undertreatment, which is the main reason for such poor efficiency of the devices. In any case, the results of the nonuniform treatment make the analysis complicated, so further examination focuses only on the red region of any characterized substrate, which proved to be the region best affected by $CdCl_2$ flow (Figure 21 *a*).

Unfortunately, all devices with the nanostructured layers were destroyed on annealing at 425 °C for 30 min, similar to the annealed QDs described in the previous section. After the heat exposure, the deposited layers were characterized by large pinholes of size of a millimeter resulting in complete loss of device function. Because of the destruction of the films, it was not possible to perform I-V measurements on these devices.

In order to obtain more information on the $CdCl_2$ effect on the structures examined, a second fabrication run was performed for each structure but with decreased duration of $CdCl_2$ treatment. The effect of the treatment reduction for control devices from 30 min to

20 min is illustrated in Figure 23 and Table III. The efficiency of the control devices is reduced by an order of magnitude with reduction of $CdCl_2$ exposure.

On the other hand, cells made with films having the structure *b* have not suffered so severely from the lack of adhesion as was the case for annealing time of 30 min. The functionality of these devices with the CdSe and the CdS quantum dots was still preserved even though their efficiencies were extremely low (Figure 24 *a*). The structure *b* devices with the Au dots showed a resistor-like behavior (Figure 24 *b*). Finally, all the devices of structure *c* were destroyed in cases of both 30 min and 20 min annealing treatment. The comparison between structure *b* and structure *c* devices shows that not only the annealing time affects the adhesion properties of the nanocrystalline layer but also interfacial properties with the surrounding layers play an important role as well.

4.5.3. Summary of results

The maximum achieved conversion efficiency in case of the control devices is only 2.3 %. This low efficiency is reflected by relatively low short circuit current density J_{sc}, and low fill factor *FF*, caused by low shunt resistance R_{SH} and high series resistance R_S. Additionally, the open circuit voltage V_{OC} of 0.6 V is below the expected range of 0.7 - 0.8 V for the higher performing devices.

The nanocrystalline layers formed by drop-casting colloidal quantum dots of Au, CdSe, and CdS appear to have a form of closely packed irregularly ordered clusters of a range of sizes from nanoscale to micro-scale. Because of the size and periodicity irregularities, these clusters merge together at moderate and high temperatures forming larger, millimeter-scale chunks that often peel off the substrate.

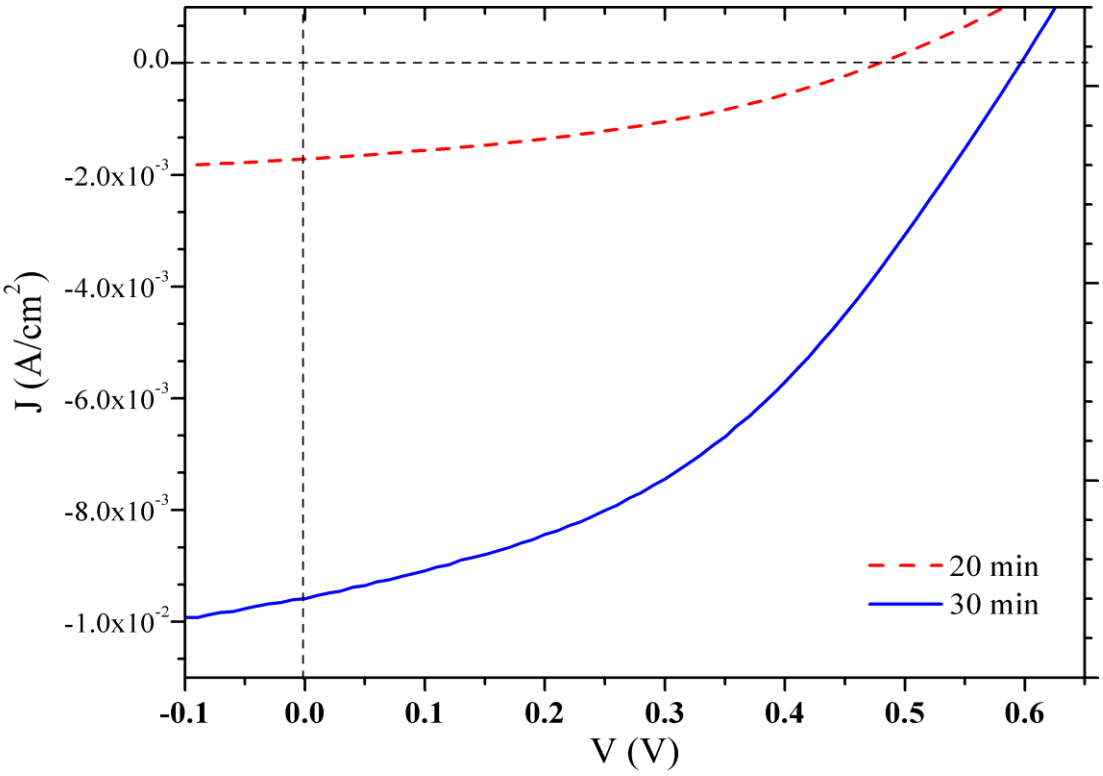

Figure 23. Effect of $CdCl_2$ treatment duration on control devices

Table III I-V parameters of the control cells treated with $CdCl_2$ vapor for 20 and 30 min

Parameter	20 min $CdCl_2$ treatment	30 min $CdCl_2$ treatment
V_{OC}	0.47 V	0.60 V
J_{SC}	1.7 mA/cm^2	9.6 mA/cm^2
R_{SH}	650 Ω	230 Ω
R_S	~ 100 Ω	30 Ω
V_{max}	0.29 V	0.35 V
J_{max}	1.1 mA/ cm^2	6.7 mA/ cm^2
FF	38.1 %	40.7 %
eff	0.3 %	2.3 %

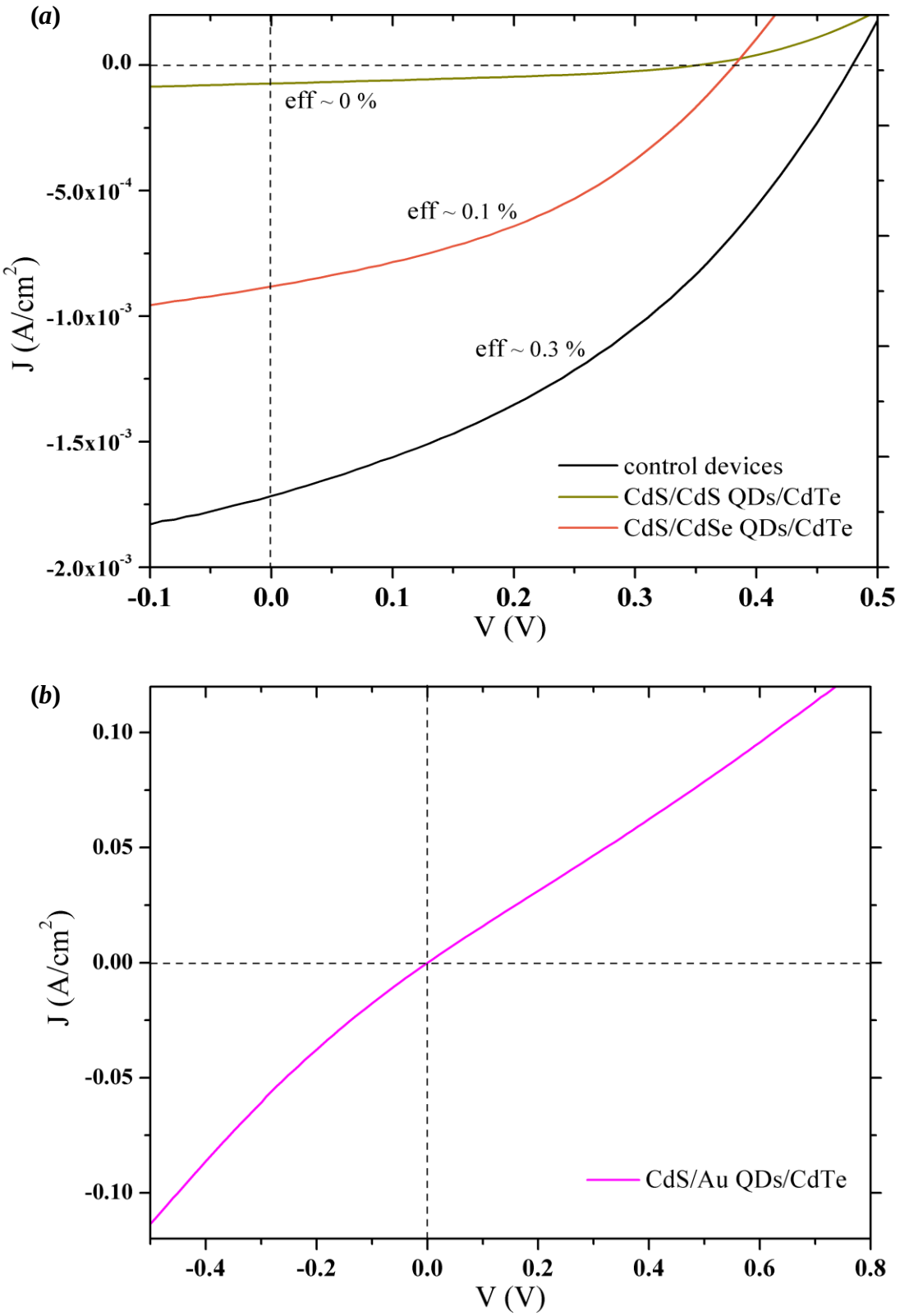

Figure 24. I-V characteristics of the structure *b* devices treated with $CdCl_2$ vapor for 20 min: (*a*) low efficiency of CdS and CdSe QD containing cells and (*b)* resistor-like behavior of Au QD containing devices

Table IV Summary of the results

Type of structure		$CdCl_2$ treatment duration: 20 min	$CdCl_2$ treatment duration: 30 min
Control devices:	CdS/ CdTe	eff ~ 0.3 %	eff ~ 2 %
Structure *b*:	CdS/Au_QD/CdTe	Resistor-like behavior	Adhesion issues
	CdS/CdS_QD/CdTe	eff ~ 0 %	Adhesion issues
	CdS/CdSe_QD/CdTe	eff ~ 0.1 %	Adhesion issues
Structure *c*:	Au_QD/CdS /CdTe	Adhesion issues	Adhesion issues
	CdS_QD/CdS /CdTe	Adhesion issues	Adhesion issues
	CdSe_QD/CdS /CdTe	Adhesion issues	Adhesion issues

When these layers are inserted in a CdTe cell structure, they are severely affected by the $CdCl_2$ treatment performed at 425 °C, resulting in degraded cell performance or even total destruction of the structure. Longer annealing times lead to more severe degradation of devices containing a nanostructured layer while they improve performance of the control devices. These competing conditions are the major obstacle in realization of a nanostructured CdTe solar cell with enhanced efficiency.

Additionally, the nature of interfaces between the nanocrystalline and surrounding layers affects the degree of degradation of the structure. The nanocrystalline layers of the structure *c* are more severely affected by adhesion issues than those from the structure *b*.

The summary of the results for each of the fabricated structure treated with $CdCl_2$ for 20 min and 30 min is presented in Table IV.

5. BLOCK COPOLYMER LITHOGRAPHY

BCP thin films have significant potential to be used as either active nanostructured layers or sacrificial templates for nanostructures in optoelectronic applications.[23] Special interest in this class of materials arises due to their ability to self-assemble on the nanoscale. Highly tunable self-assembly provides an inexpensive approach to formation of various kinds of highly ordered nanoscale morphologies that are capable of improving performance of various optoelectronic devices. Therefore, BCP lithography is a possible approach to assemble uniform matrices of metallic, inorganic or organic nanoparticles on a variety of substrates that can be beneficial in a number of photovoltaic applications.

5.1. Block copolymers

BCPs are widespread materials present in a variety of products such as adhesive tape, upholstery foam, asphalt additives, etc. These are soft materials with a fluid-like disorder at the molecular level, characterized by complex structures and a variety of useful properties.

BCPs are macromolecules composed of two or more covalently bonded but chemically distinct homopolymer chains referred to as blocks. They are classified by number of distinct blocks and type of linkage between them (linear vs. branched). Chemical incompatibility of the blocks drives their segregation, but it is counterbalanced by forces of covalent bonds. As a result, the phase separation happens on the nanoscale rather than

on a bulk level. Consequently, the polymer blocks self-assemble into highly ordered and periodic nanodomains with a variety of morphologies.

A typical example of BCP is a linear AB diblock copolymer formed from two distinct blocks, A and B. The incompatibility between the blocks is characterized with the Flory-Huggins interaction parameter:

$$\chi_{AB} = \frac{Z}{k_B T}\left[\varepsilon_{AB} - \frac{1}{2}(\varepsilon_{AA}+\varepsilon_{BB})\right] \quad (9)$$

In this equation, Z represents a scaling factor, ε_{AB} is interaction energy per monomer between monomers A and B, and ε_{AA} and ε_{BB} are self-interaction energies among blocks A and B, respectively. In most cases χ_{AB} is a positive number indicating repulsion between blocks, while a negative value would signify mixing of the blocks.

Phase separation and morphology of linear diblock copolymer bulk structures are affected mainly by two factors: (i) $\chi_{AB}N$, where N is the overall degree of polymerization, and (ii) f_A, standing for the fraction of block A in the BCP. Effects of the two factors are best described by the phase diagram shown in Figure 25.[24] Higher $\chi_{AB}N$ factor implies better promotion of the phase separation. In order to induce the phase separation, a BCP material must have sufficient mobility, which can be achieved with temperature or solvent absorption. On the other side, the temperature should not exceed the order-disorder temperature (ODT) limit in order to avoid formation of a disordered melt. It is important to notice that the $\chi_{AB}N$ factor is inversely proportional to the temperature and that the phase separation takes place only in the region above the ODT curve.

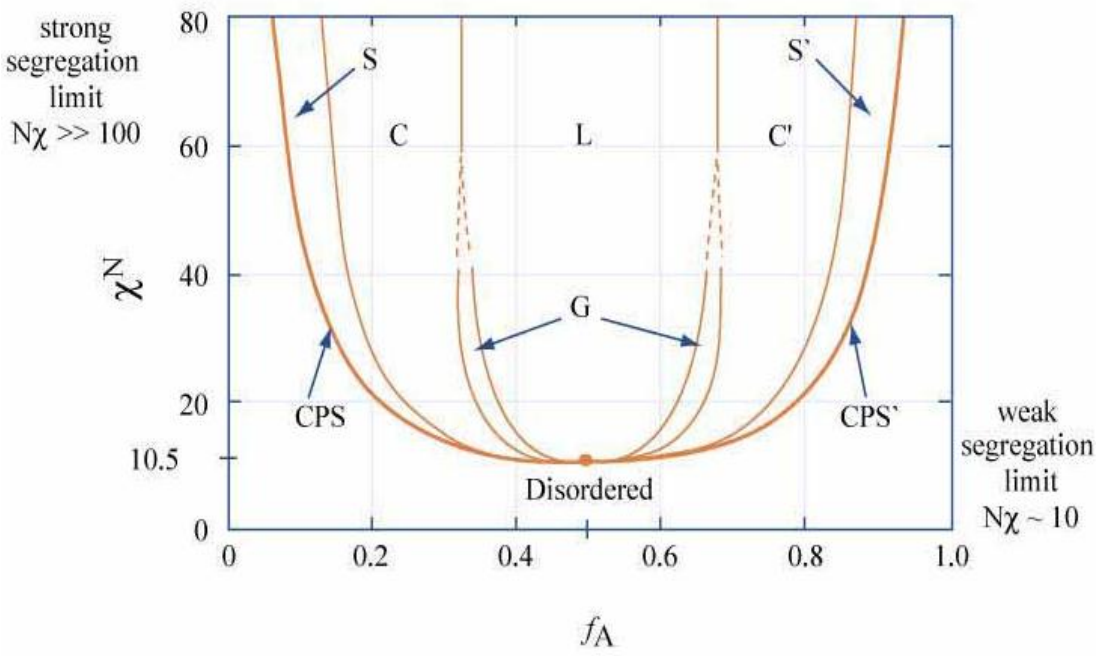

Figure 25. Diblock copolymer morphology diagram. Source: MIT OpenCourseWare, http://www.flickr.com/photos/mitopencourseware/3323137283/

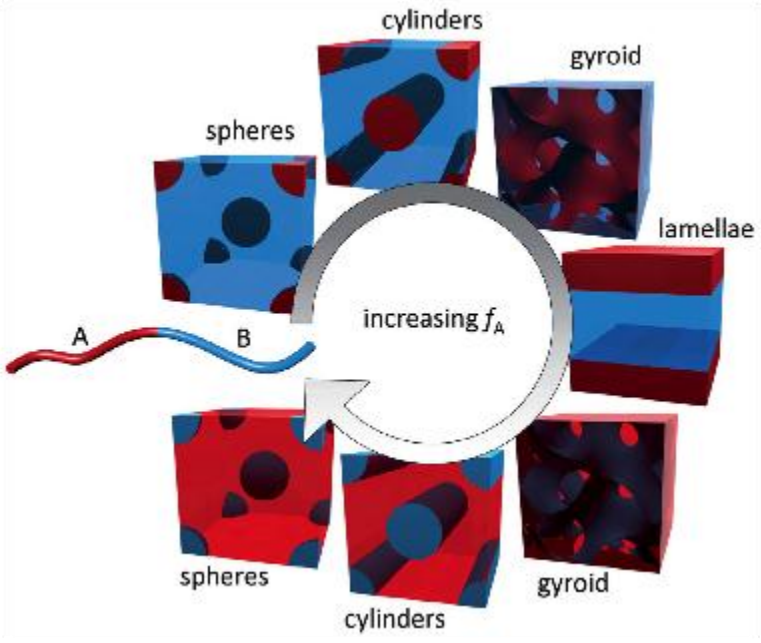

Figure 26. 3-dimensional representation of diblock morphologies as a function of f_A. Source: Seth B. Darling.[23]

Morphology of the structure also depends on the composition f_A. Lamellar phase (L) is stable for compositionally symmetric diblocks while cylindrical phase (C) is characteristic for intermediate levels of compositional asymmetry. In a narrow region between L and C phases and close to the ODT curve, a complex gyroid phase (G) is stable. Finally, body-centered spherical phase (S) is stable for highly asymmetric compositions while closely packed spheres (CPS) are formed in the case of extremely high levels of asymmetry. The common morphologies of a diblock copolymer as a function of the composition f_A are illustrated in three dimensions in Figure 26.

5.2. Block copolymer thin films

As the thickness of a diblock copolymer film decreases, the polymer-polymer interactions providing the order become less prominent and the influence at the interfaces of the film become more significant. As a result, achievement of an ordered structure of a particular morphology in a thin BCP film requires consideration of an additional parameter: interfacial interactions of the film.

Interfacial interactions have a crucial influence on morphology of thin BCP films. For example, in the case of moderately asymmetric BCPs, a morphology comprised of in-plane cylinders, parallel to the substrate, is expected as a result of preferential wetting of the interfaces. However, if the film is extremely thin, cylinders oriented perpendicular to the substrate can be achieved in certain systems. In order to controllably obtain standing cylinders in a thin BCP film, there should be balanced interfacial interactions of the blocks with the substrate and the free surface.

There are several ways to neutralize the effect of surface interactions on morphology of thin BCP films. The most common approaches include surface modification via random copolymer (RCP), annealing under external fields, solvent annealing, and surface patterning. Surface modification via RCP is the most robust and versatile approach adaptable to a wide range of polymer materials.[25] Using this technique, the surface energy of the substrate is controlled by tuning the relative composition of the RCP, and thus can be optimized for a particular BCP. Examples of in-plane, mixed and standing cylinders are shown in Figure 27.

Once a desired morphology is obtained, one of the blocks can be removed by a selective etching process. In many applications in which the BCP will be used as a deposition mask for the fabrication of nanodots, vertically oriented cylinders are desired where the cylinders are comprised of the block that will etch more quickly.

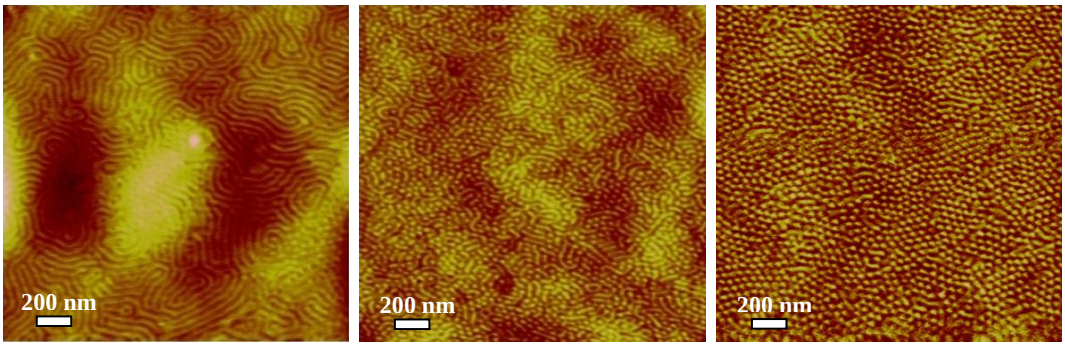

Figure 27. AFM topography images of in-plane (*a*), mixed (*b*) and standing (*c*) cylinders of PS-*b*-PMMA on ITO substrate

5.3. Uniform Au nanoparticles on ITO substrate

This section describes procedure of obtaining a nanoengineered template on ITO-coated glass, which can be used as a sacrificial layer for fabrication of a highly ordered and densely packed matrix of metallic nanoparticles. The diblock copolymer used in this experiment was PS-*b*-PMMA. The weight composition of the BCP was about 70% polystyrene (PS) and 30% poly(methyl methacrylate) (PMMA), which is a moderately asymmetric composition resulting in cylindrical phase separation. The cylinders are formed from the minority PMMA blocks and they are surrounded by a matrix of majority PS blocks. PS-*b*-PMMA thin films were applied onto ITO substrates by spin-coating solutions in toluene. Direct application of PS-*b*-PMMA thin films on the substrate resulted in formation of undesired in-plane or mixed cylinders regardless of the film thickness and annealing conditions. The reason for this was unbalanced interfacial interactions of PS and PMMA blocks with the ITO substrate. Because of this phenomenon, surface modification was performed using PS-*r*-PMMA random copolymer with composition of 0.59 for the PS block. This treatment was engineered to render the substrate neutral to the PS and PMMA blocks. After the surface was neutralized, the film thickness was tuned until a structure of standing cylinders was obtained.

In the next step, the structure of standing PMMA cylinders in PS matrix was subject to reactive ion etching (RIE). Since PMMA features a higher etching rate when subject to oxygen-based RIE, it will be removed faster than the PS portion of the film. Eventually, PMMA cylinders are completely etched leaving behind a PS matrix with densely packed nanoscale holes. The etching conditions are established by varying the etching time and analyzing the corresponding ATR-FTIR data. A detailed procedure for fabrication of the

template is described in Table V. AFM images of the PS-*b*-PMMA before and after RIE treatment are shown on Figure 28. Figure 29 illustrates normalized amounts of PS and PMMA as a function of etching time.

Once a nanoporous PS template was formed on the ITO substrate, a 5 nm thin Au film was deposited over the template using e-beam deposition. The Au film had an easily observable grey color. The next step in the process is to remove the PS mask and the gold on top of the mask using a lift-off technique; if the sample is treated with a chemical that etches PS, the polymer matrix, together with the overlaying Au should be successfully removed. Portions of the Au film that fill the holes of the matrix should stay attached to the substrate. As a result, a matrix of densely packed Au nanoparticles should be assembled on the ITO substrate.

A number of PS etching chemistries were explored, and the only etchant that completely removed the polymer from the substrate was photoresist (PR) remover 1165. Therefore, a lift-off of the Au films deposited over the PS templates has been attempted with the PR remover. As a result, the grey color of Au disappeared and AFM images revealed a distribution of densely packed nano-sized dots of about 20 nm in diameter, very similar to the inversed pattern of the PS matrix. Analysis of these nanodots arrays is currently underway.

Table V Process summary for fabrication of nanostructured templates via PS-PMMA block copolymer

Processing step	Comment
1. Preparation of ITO substrate:	
• Soap clean.	• Removes larger contaminating particles.
• DI H_2O rinse.	
• Hot plate: 65 °C, 2.5 hrs 30% H_2O_2 / 30% NH_3OH / DI H_2O (1/1/5).	• Generates OH bonds on ITO to be linked to RCP.
• Submerge into DI H_2O.	• Protects the OH bonds from air exposure.
• Air gun dry.	• Prior film application.
2. Neutralization of ITO surface:	
• Solution: 1% of PS-r-PMMA in toluene, f_{PS}= 0.59.	
• Spinner: 100 ml, 2000 rpm, 40 sec.	• Forms 35-40 nm thick film
• Hot plate in N_2 atm.: 240 °C, 40 min.	• Promotes linking of the bottom 2-5 nm of the film to the OH bonds on ITO
• Spinner: toluene rinse 3X, 100 ml, 4500 rpm, 40 sec.	• Removes the unlinked portion of the film
3. Application of PS-PMMA film	
• Solution: 1% of PS-b-PMMA in toluene, f_{PS}= 0.70.	
• Spinner: 75 ml, 2500 rpm, 40 sec.	• Forms ~ 30 nm thick film
• Vacuum oven: 180 °C, 24 hrs, under vacuum.	• Promotes phase separation: formation of standing PMMA cylinders in PS matrix
4. Selective etching of PMMA cylinders	
• RIE (March): power = 40W, pressure = 160 Torr, O_2 flow = 22, time = 42 sec.	• PMMA cylinders are removed at a faster rate than PS matrix
• Acetic acid etch: 30% concentrated, 5 min.	• Removes remaining dangling bonds of PMMA
• Methanol soak: 20 min.	• Rinses the sample from acetic acid
• Air gun dry.	

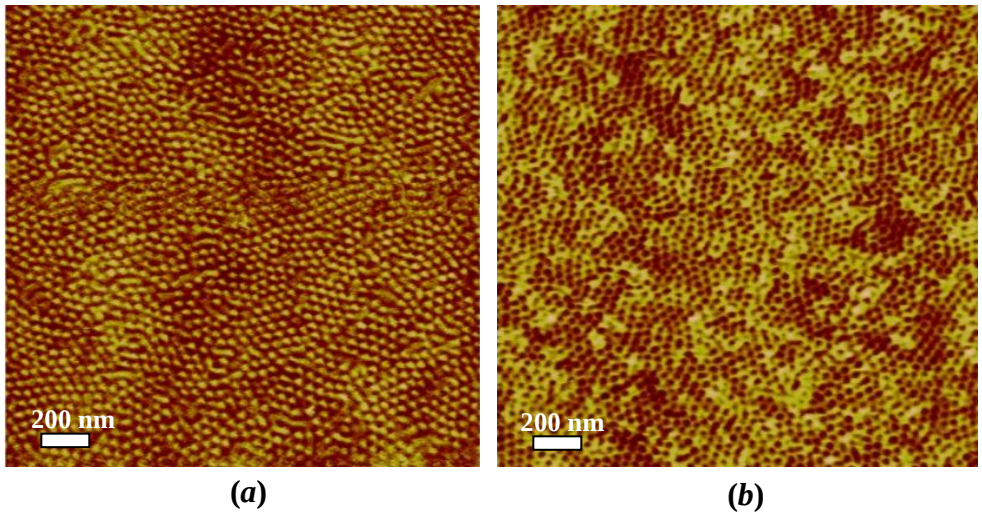

Figure 28. AFM topography images of (*a*) standing PMMA cylinders in the PS matrix on ITO before RIE and (*b*) PS matrix on ITO after removal of PMMA cylinders via RIE

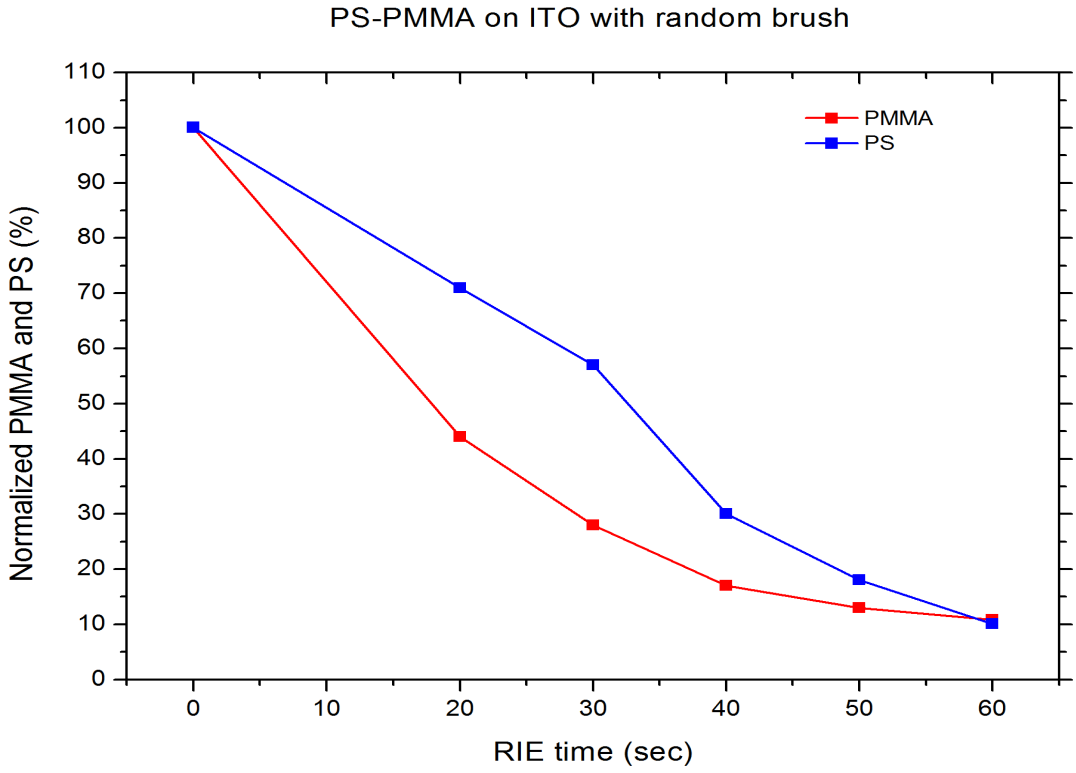

Figure 29. Normalized amounts of PS and PMMA remained after various RIE times

6. FUTURE WORK

6.1. CdTe solar cells with nanocrystalline layer

First, the proposed concepts for efficiency enhancement should be tested on cells fabricated in a subrstrate configuration. Despite to lower record efficiency achieved for this type of the structure, the potentials of the proposed mechanisms are expected to be more obvious because the exposure of nanocrystalline layers to high temperatures is avoided in this case. Also, the $CdCl_2$ treatment needs to be optimized to a uniform and controllable process in order to obtain a control over passivation of the defects in the CdTe absorber. The vapor $CdCl_2$ process can be replaced by a vacuum deposition of a thin $CdCl_2$ film on the absorber followed by a post annealing treatment.

Secondly, the structure of nanocrystalline layers should be optimized. Layers of regularly spaced nanoparticles rather than layers of disordered clusters composed of particles of a variety of sizes are desired; this way, interfacial defects may be minimized. Drop-casting methods should be replaced by a nontraditional, inexpensive deposition technique. One of the approaches, especially for assembly of metallic nanostructures, is block copolymer lithography, a lithographic process described in the previous chapter. Once a robust procedure for assembly of highly ordered nanocrystalline layers is established, it should be utilized for fabrication of the nanoengineered CdTe cells. In this case, the comparison between the standard CdTe solar cells and their nanoengineered counterparts should be more conclusive.

6.2. Uniform Au nanoarrays on ITO substrate

Firstly, the material composition of the nanoparticles formed on ITO after treating the Au films with the PR remover needs to be identified. If it turns out that these are actually Au dots, this task is completed. Otherwise, further investigations need to be done; other parameters should be considered such as chemicals used for the lift-off, different thicknesses of the Au film, various etching times, or addition of an adhesion layer such as Cr or Ti prior to the Au deposition.

Once the process of obtaining Au nanodots on ITO is established, dimensional features of the matrix can be tuned with choice of an appropriate version of PS-*b*-PMMA. Following the procedure from Table V and choosing a different molecular weight of PS-*b*-PMMA while the ratio of molecular weights between PS and PMMA is kept constant, would result in a different size of the domains.[26] Therefore, dimensional features of the Au QDs can be optimized for specific applications.

6.3. Nanoengineered hybrid CdS/polymer solar cell

The matrix of Au QDs is planned to be utilized for fabrication of a hybrid CdS/P3HT solar cell (Figure 30). The Au QDs on ITO can serve the purpose of a catalyst for vapor-liquid-solid (VLS) growth of CdS nanorods, which can subsequently be surrounded with a conjugated polymer matrix. The advantages of making the Au dots using BCP lithography rather than using a traditional approach are high density, high order, close

packing, and dimensional control of the particles that results in improved characteristics of the grown arrays of CdS nanorods. These improved features should enhance the benefits of three-dimensional cell structures such as enhanced absorption efficiency of the material, and improved photocarrier separation and collection,[27] thus resulting in higher conversion efficiency.

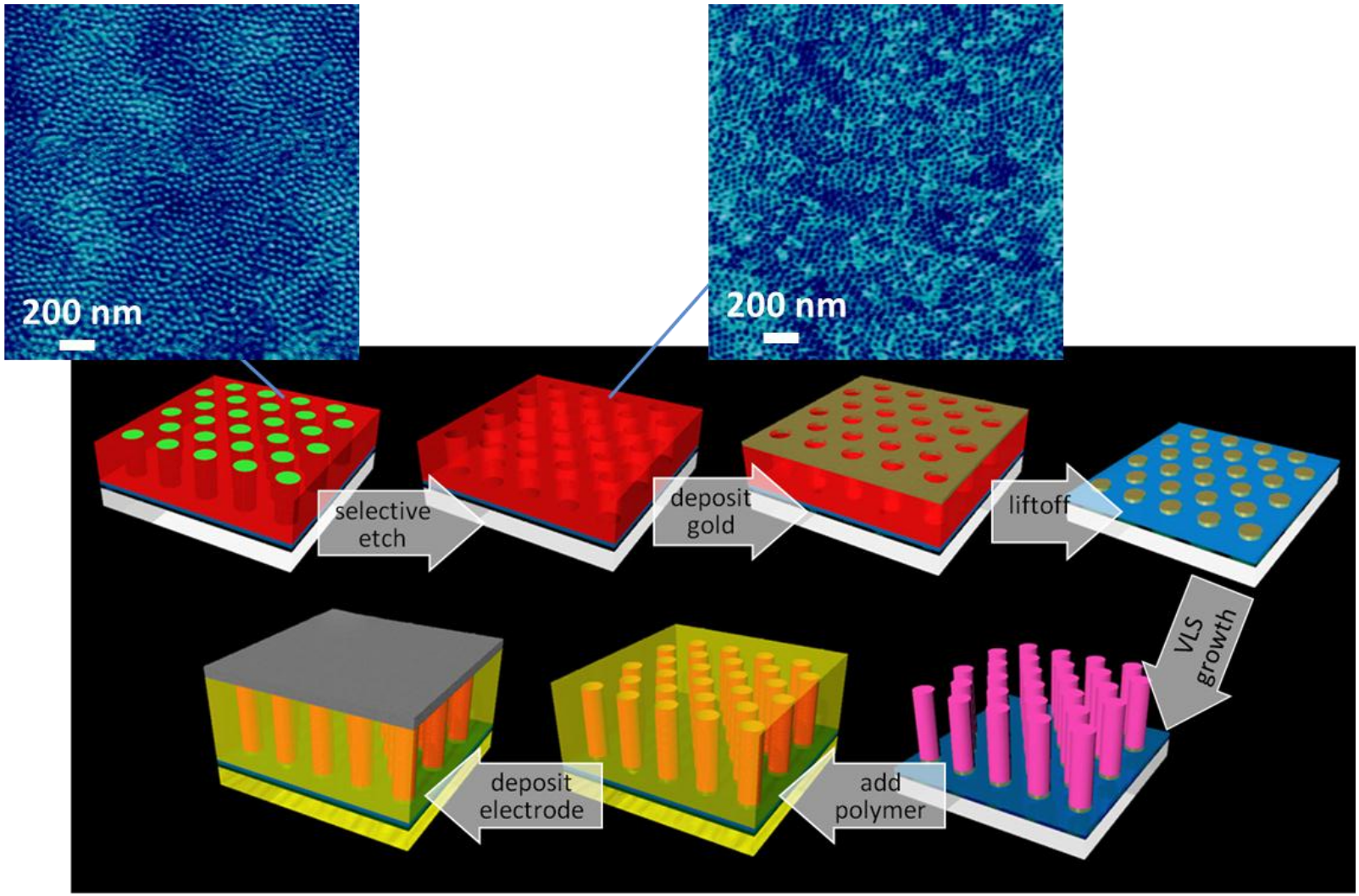

Figure 30. Processing steps for a hybrid CdS/P3HT solar cells via BCP lithography

CITED LITERATURE

[1] U.S. Energy Information Administration. 2010 International Energy Outlook. " World Energy Demand and Economic Outlook." Internet: http://www.eia.gov/oiaf/ieo/world.html, Jul. 27, 2010 [Jun. 29, 2011].

[2] Wikipedia. "Wind Power." Internet: http://en.wikipedia.org/wiki/Wind_power, Jul. 3, 2011 [Jul. 10, 2011].

[3] Atoms for Peace Energy Conference. Energy Resources. "Solar Energy." Internet: http://www.ifpaenergyconference.com/Solar-Energy.html, Oct. 22, 2003 [Jun. 29, 2011].

[4] K.-S. Liao, S. D. Yambem, A. Haldar, N. Alley and S. A. Curran. "Design and Architectures for the Next Generation of Organic Solar Cells." *Energies*, vol. 3, pp. 1212-1250, Jun. 2010.

[5] K. L. Chopra, P. D. Paulson and V. Dutta. "Thin-Film Solar Cells: An Overview." *Progress in Photovoltaics: Research and Applications*, vol. 12, pp. 69-92, Mar.-May. 2004.

[6] J. Fahey. "GE jumps into the solar panel business with plans to build a big plant," *USA Today*. Internet: http://www.usatoday.com/money/industries/energy/2011-04-07-ge-solar-panel-plant.htm, " Apr. 8, 2011 [June 29, 2011].

[7] KACO new energy. "Glossary." Internet: http://www.kaco-newenergy.com/index.php?option=com_content&view=article&id=102 [June 29, 2011].

[8] J. Fritsche, D. Kraft, A. Thissen, T. Mayer, A. Klein, W. Jaegermann. "Band energy diagram of CdTe thin film solar cell." *Thin Solid Films*, vol. 403–404, pp. 252-257, 2002.

[9] M. Burgelman. "Cadmium Telluride Thin Film Solar Cells: Characterization, Fabrication and Modeling," in *Thin Film Solar Cells: Fabrication, Characterization and Applications*. J. Poortmans and V. Arkhipov, Ed. Chichester: John Wiley & Sons, 2006, pp. 277-324.

[10] E. Molva, J. P. Chamonal, and J. L. Pautrat. "Shallow acceptors in cadmium telluride." *Physica Status Solidi B*, vol. 109, pp. 635-644, Feb. 1982.

[11] J. Pautrat and N. Magnea. "Shallow and deep levels in Zn/Cd/Te/Se compounds," in *Narrow Gap Cadmium Based Compounds*, vol 13. P. Capper, Ed. London: INSPEC, 1994, pp. 546-554.

[12] Y. Marfaing. "Impurity doping and compensation mechanisms in cadmium telluride." *Thin Solid Films*, vol. 387, pp. 123-128, May 2001.

[13] M.D.G. Potter, D.P. Halliday, M. Cousins, and K. Durose. "A study of the effects of varying cadmium chloride treatment on the luminescent properties of CdTe/CdS thin film solar cells." *Thin Solid Films*, vol. 361-362, pp. 248-252, 2000.

[14] K.K. Chin. "p-Doping limit and donor compensation in CdTe polycrystalline thin film solar cells." *Solar Energy Materials & Solar Cell*, 2010, doi:10.1016/j.solmat.2010.05.006.

[15] Kevin D. Dobson, I. Visoly-Fisher, G. Hodes, and D. Cahen. "Stability of CdTe/CdS thin-film solar cells." *Solar Energy Materials & Solar Cells*, vol. 62, pp. 295-325, May 2000.

CITED LITERATURE (continued)

[16] I. M. Kotinay, L. M. Tukhkoneny, G. V. Patsekinay, A. V. Shchukarevzand G. M. Gusinskii. "Study of CdTe etching process in alcoholic solutions of bromine." *Semiconductor Science and Technol*ogy, vol. 13, pp. 890–894, Aug. 1998.

[17] D W Palmer. "Properties of the II-IV Semiconductors." Internet: www.semiconductors.co.uk, 2008 [Jun. 30, 2011].

[18] H. Föll. " Elements of Advanced Theory - Effective Masses." Internet: http://www.tf.uni-kiel.de/matwis/amat/semi_en/kap_2/backbone/r2_3_1.html, 2008 [Jun. 30, 2011].

[19] W. Shockley and H. J. Queisser, "Detailed Balance Limit of Efficiency of p-n Junction Solar Cells." *Journal of Appied. Physics*, vol. 32, 510-519, Mar. 1961.

[20] A. Marti, E. Antolin, C. R. Stanley, C. D. Farmer, N. Lopez, P. Diaz, E. Cánovas, P. G. Linares, and A. Luque. "Production of Photocurrent due to Intermediate-to-Conduction-Band Transitions: A Demonstration of a Key Operating Principle of the Intermediate-Band Solar Cell." *Physical Review Letters*, vol. 97, pp. 247701-247704, Aug. 2006.

[21] A. J. Haes and R. P. V. Duyne. "Preliminary studies and potential applications of localized surface plasmon resonance spectroscopy in medical diagnostics." *Expert Rev. Mol. Diagn*, vol. 4, pp. 527–537, 2004.

[22] A. Luque, A. Marti and A. J. Nozik. "Solar Cells based on Quantum Dots: Multiple Exciton Generation and Intermediate Bands." *MRS Bulletin* , vol. 32, pp. 236-241, 2007.

[23] I. Botiz, S. B. Darling, "Optoelectronics using block copolymers." *Materials Today*, vol. 13, pp. 42-51, May 2010.

[24] MIT OpenCourseWare. "Diblock Morphology Phase diagram." Internet: http://www.flickr.com/photos/mitopencourseware/3323137283/, [Jun. 30, 2011].

[25] D. Y. Ryu, S. Ham, E. Kim, U. Jeong, C. J. Hawker, T. P. Russell. "Cylindrical Microdomain Orientation of PS-*b*-PMMA on the Balanced Interfacial Interactions: Copmosition Effect of Block Copolymers." *Macromolecules*, vol. 42, pp. 4902-4906, May 2009.

[26] T. Xu, H.-C. Kim, J. DeRouchey, C. Seney, C. Levesque, P. Martin, C. M. Stafford, T. P. Russell. "The influence of molecular weight on nanoporous polymer films." *Polymer*, vol. 42, pp. 9091-9095, Jul. 2001.

[27] Z. Fan, H. Razavi, J. Do, A. Moriwaki, O. Ergen Y.-L. Chueh, P. W. Leu, J. C. Ho, T. Takahashi, L. A. Reichertz, S. Neale, K. Yu, M. Wu, J. W. Ager and A. Javey. "Three-dimensional nanopillar-array photovoltaics on low-cost and flexible substrates." *Nature Materials*, vol. 8, pp. 648-653, Jul. 2009.

VITA

NAME: Rade Kuljic

EDUCATION: M.S., Electrical and Computer Engineering, University of Illinois, Chicago, Illinous, 2011.

B.S., Electrical Engineering, Highest Honors, University of Illinois, Urbana-Champaign, Illinois, 2009.

TEACHING: Department of Electrical and Computer Engineering, University of Illinois, Chicago, Illinois. EXPERIENCE: Electronics Instructional Laboratories: Fabrication and Characterization of Microelectromechanical system (MEMS) based devices, 2011.

HONORS The Bronze Tablet Recepient, University of Illinois at Urbana-Champaign, 2009.

Highest Honors Award, Department of Electrical and Computer Engineering, University of Illinois at Urbana-Champaign, 2009.

Jules D. Falzer Scholarship, University of Illinois at Urbana-Champaign, 2008.

Henry O. Koehler Memorial Scholarship, University of Illinois at Urbana-Champaign, 2007.

WORKING EXPERIENCE: Laboratory Graduate Assistant, Center for Nanoscale Meterials, Argone National Laboratory, Lemont, Illinois, May 2010 – Aug 2011.

Research Assistant, Department of Electrical and Computer Engineering, University of Illinois, Chicago, Illinois, Jun. 2009 – Dec. 2010.

Test Engineer, Intern, Analog Devices Inc., Wilmington, Massachusetts, May 2008 – Aug. 2008.

VITA (continued)

PUBLICATIONS:

K. G. Punchihewa, E. Zaker, R. Kuljic, K. Banerjee, T. Dankovic, A. Feinerman, and H. Busta. "Improvement of the Sensitivity and Operating Range of MEMS-based Resistive-type Vacuum Gauges." To be submiotted in *Journal of Micromechanics and Microengineering*.

R. Kuljic, J. Chang, N. Jayapratha, T. Dankovic, K. Banerjee, A. Feinerman, H. Busta. "Microelectromechanical system-based vacuum gauge for measuring pressure and outgassing rates in miniaturized vacuum microelectronic devices." *Journal of Vacuum Science & Technology B: Microelectronics and Nanometer Structures*, vol. 29, pp. 02B114-1 - 02B114-5, Mar. 2011.

H. Jung, R. Kuljic, M. A. Stroscio, and M. Dutta. "Confinement in PbSe wires grown by rf magnetron sputtering." *Applied Physics Letters*, vol. 96, pp. 153106-1 – 153106-3, Apr. 2010.